Nonlinear wakes behind a row of elongated roughness elements

M. E. Goldstein[1], Adrian Sescu[2], Peter W. Duck[3] and Meelan Choudhari[4]

[1]National Aeronautics and Space Administration, Glenn Research Center, Cleveland, OH 44135, USA

[2]Mississippi State University, Department of Aerospace Engineering, Mississippi State, MS 39762, USA

[3]University of Manchester, School of Mathematics, Manchester, M13 9PL, U. K.

[4]National Aeronautics and Space Administration, Langley Research Center, Hampton, VA, 23681, USA

This paper is concerned with the high Reynolds number flow over a spanwise periodic array of roughness elements with inter-element spacing of the order of the local boundary-layer thickness. While earlier work by Goldstein, Sescu, Duck and Choudhari (2010) and Goldstein, Sescu, Duck and Choudhari (2011) was mainly concerned with smaller roughness heights that produced relatively weak distortions of the downstream flow, the focus here is on extending the analysis to larger roughness heights and streamwise elongated planform shapes that together produce a qualitatively different, nonlinear behavior of the downstream wakes. The roughness scale flow now has a novel triple-deck structure that is somewhat different from related studies that have previously appeared in the literature. The resulting flow is formally nonlinear in the intermediate wake region, where the streamwise distance is large compared to the roughness dimensions but small compared to the downstream distance from the leading edge, as well as in the far wake region where the streamwise length scale is of the order of the downstream distance from the leading edge. In contrast, the flow perturbations in both of these wake regions were strictly linear in the earlier work by Goldstein et al (2010, 2011). This is an important difference because the nonlinear wake flow in the present case provides an appropriate basic state for studying the secondary instability and eventual breakdown into turbulence.

1. Introduction

It is generally agreed that the streaks induced by 3D distributed surface roughness play an important role in the so called *bypass* transition that often occurs in linearly stable or weakly unstable boundary-layer flows. In fact, it is well-known that certain types of streak-like perturbations of linearly stable shear flows may undergo a transient algebraic growth prior to an eventual exponential decay (Case, 1960; Ellingson & Palm, 1975; Landahl, 1980). It is, therefore, important to understand the physical mechanisms related to potential disturbance growth in the wake flow behind the surface roughness.

Ergin and White (2006) investigated the steady and unsteady disturbances generated by a spanwise array of cylindrical roughness elements in the context of transient algebraic growth. They found that the steady disturbance energy decreases rapidly just behind the roughness element with transient growth occurring further downstream. But transition to turbulence resulting from rapid exponential growth of secondary instabilities only occurred for larger roughness Reynolds numbers. They concluded that the transition behind the roughness

elements can be viewed as a competition between the unsteady secondary disturbance growth and the relatively fast relaxation of the basic steady flow toward a spanwise uniform Blasius flow. Rapid transition occurs when the steady disturbance generated by the roughness element is large because the unsteady secondary instabilities are then able to reach transitional amplitudes before the steady disturbance induced by the roughness elements relaxes to a stable state.

Algebraic or non-modal growth is believed to arise from the "lift-up" effect associated with spanwise varying displacement of a 2D shear flow (Stuart, 1965; Case, 1960; Landahl, 1980). This phenomenon is typically found to take place over streamwise length scales that are comparable to the downstream distance from the leading edge (e.g., Andersson et al.,1999), but Goldstein, Sescu, Duck and Choudhari (2011, hereafter referred to as GSDC-2), showed that a purely transcendental (algebraic/logarithmic) growth can occur on a much shorter streamwise length scale that is large compared to the roughness elements themselves, but small compared to the distance from the leading edge. Non-modal growth over the longer streamwise length scale is best characterized as transient growth since the disturbance eventually decays on the same scale.

Experiments by Fransson et al. (2004) have shown that steady (and stable) laminar streaks are capable of delaying transition by decreasing or eliminating the growth of Tollmien–Schlichting (T-S) waves without introducing streak instabilities. Fransson et al. (2004) also found that the stabilization of T-S disturbances increases with increasing streak amplitude for a prescribed spanwise periodicity of the streaks. They were able to obtain steady streak amplitudes of up to 12% of the free stream velocity using roughness elements with circular planform, while Fransson and Talamelli (2012) were recently able to use vortex generators to generate stable streaks of even larger amplitudes.

GSDC-2 and Goldstein, Sescu, Duck and Choudhari (2010, hereafter referred to as GSDC-1) obtained an asymptotic high-Reynolds-number solution for the flow over a spanwise periodic array of relatively small roughness elements whose spanwise separation and plan form dimensions are of the order of the local boundary-layer thickness δ^*. They showed that the local flow in the vicinity of the roughness has a double layer structure that is the same as in Choudhari and Duck (1996). But this result becomes invalid over downstream distances comparable to the distance, say x_0^*, from the leading edge. Non-parallel effects come into play in this region and the flow is governed by the Boundary Region Equations (BRE) of Kemp (1951). The numerical results show that the wake velocity perturbations exhibit transient growth in the BRE region, but the flow perturbations always remained linear in this region even when the flow is nonlinear in the vicinity of the roughness elements. The earlier studies (Stuart, 1965; Case, 1960; Landahl,1980) only considered exactly parallel base flows with inviscid streaks that exhibited purely temporal growth and were completely independent of the streamwise coordinate. Case (1960), for example, analyzed the initial value problem for small amplitude disturbances on linearly stable parallel shear flows and showed that certain types of streak-like perturbations can grow algebraically in time before exhibiting exponential decay.

Calculations presented in GSDC-1 and GSDC-2 suggest that the roughness elements with the largest roughness heights produced flows that develop recirculating flows immediately downstream of the roughness elements which are likely to break down and initiate vortex shedding before the streak amplitudes can become large enough to produce $O(1)$ changes in the downstream flow. But (as shown in section 7, below) the breakdown of the recirculating flow can

be made to occur at larger roughness heights by increasing the aspect ratio of the roughness elements (i.e., making them more elongated in the streamwise direction) and therefore decreasing the slope of their downstream surfaces. The elongated elements can also provide a better representation of the vortex generators used by Fransson and Talamelli (2012) and the roughness element shapes used by Downs and Fransson (2014).

A major purpose of the present paper is to show that streamwise elongated roughness elements can lead to a more interesting flow regime involving stationary streaks with relatively large, i.e., nonlinear amplitudes in the downstream region. The analysis is again based on an asymptotic high Reynolds number solution for the flow over a spanwise periodic array of relatively small roughness elements whose spanwise separation is of the order of the local boundary-layer thickness δ^* (Figure 1). But in order to maximize the strength of the downstream wakes while maintaining a steady flow by delaying the potential breakdown of the flow in the immediate vicinity of the roughness elements, the focus is now on roughness elements with streamwise length scales of the order of the triple-deck length scale. The increased streamwise scale causes the roughness scale flow to become interactive even though it is only slightly longer that than the $O\left(\delta^*\right)$ length scale considered in GSDC-1 and GSDC-2. More important, the resulting intermediate scale flow and therefore the BRE flow further downstream is now formally nonlinear at lowest order of approximation. It is worth noting that in the related but somewhat different context of a single roughness element in a hypersonic boundary layer, Ruban and Kravtsova (2013) have shown that a fully interactive high-Reynolds-number flow can remain nonlinear asymptotically far downstream in the viscous wake region when the roughness height is sufficiently large.

Downs and Fransson (2014) used a spanwise periodic array of streamwise elongated (i.e., rib-like) roughness elements to study the effect of their wakes on the amplification of T-S waves—presumably because the longer streamwise length scales allowed them to obtain larger amplitude steady wakes. These rib-like roughness elements had hemispherical caps and hence involved two disparate length scales corresponding to the roughness element tips and the roughness mid-region, respectively. The present paper is quite germane to this experiment, even though it only considers roughness elements with a single streamwise length scale over the entire extent of the element. It is also worth mentioning that the motivation for the Downs and Fransson (2014) experiment was the stabilization of Tollmien-Schlichting waves while that the present work may be more relevant to the study of secondary instability.

The solution for the roughness wake flow (which exhibits transient growth) is now governed by the nonlinear form of the BRE at the lowest order of approximation, and can, therefore, provide an appropriate base flow for studying the secondary instability and the eventual breakdown into turbulence that was noted by Ergin & White (2006). But, the second-order term in the BRE solution, which is $O(R^{-1/8})$ relative to the zeroth order solution and formally corresponds to the linear solution given in GSDC-2, turns out to be much larger than the leading order nonlinear contribution at the start of the BRE region (at least at the finite Reynolds numbers relevant to the experiments). The second order term can, therefore, not be entirely neglected even though its amplitude decreases with increasing downstream distance while the nonlinear term undergoes transient growth and eventually becomes dominant. Another advantage of the present scaling is that it increases the maximum allowable roughness height to the order of the triple-deck height. The nearfield flow behind the streamwise elongated roughness elements

considered in this paper directly matches onto the outer BRE flow and therefore possesses a much simpler asymptotic structure than the shorter roughness planforms with an $O(1)$ aspect ratio that were considered in GSDC-1 and GSDC-2.

The relevant problem for the streamwise elongated roughness elements is formulated in section 2 and the local solution for the flow in the main boundary layer is considered in section 3. As usual, the main-deck solution becomes invalid near the wall and the appropriate equations for the wall region are derived in section 4. The resulting triple-deck structure is rather novel in that it is a hybrid between the fully interactive and compensation regimes-which seems to be somewhat different from what previously appeared in the literature (e.g. Bogolepov & Lipatov, 1985; Duck & Burggraf, 1986; Bogolepov, 1987; Bogolepov, 1988). Its numerical solution is discussed in subsection 4.2. Section 5 considerers the asymptotic behavior of the roughness scale solution at large downstream distances and shows that this solution eventually becomes invalid at a downstream distance on the order of the streamwise length scale x_0^*. A new outer-scale solution that matches onto the inner roughness scale solution is discussed in section 6. Its numerical solution is discussed in subsection 6.4 and the results and conclusions are presented in Section 7 where it is shown that the true asymptotic behavior of the wall-layer solution can only be found by considering the fully nonlinear roughness scale solution, no matter how small the roughness height h may be. It is also shown that the roughness elements can have a circular planform at moderate Reynolds numbers when their scaled streamwise length is only slightly smaller than their scaled spanwise length. The present results are therefore expected to be directly applicable to many of the previously reported experimental roughness studies involving roughness element plan forms with an O(1) aspect ratio. The analysis can even be applied to the stable flows produced by the miniature vortex generators studied by Siconolfi, Camarri & Fransson (2015) (see also, Fransson and Talamelli, 2012), but results are only presented for smooth roughness elements in section 7. Some concluding remarks are given in section 8. The short roughness problem is revisited in Appendix C where it is shown that the present long streamwise length scale solution is also needed in order to extend the short streamwise length scale solutions of GSDC-1 and GSDC-1 into the fully non-linear intermediate scale regime.

2. Formulation and Scaling

Our interest here is in studying the transient growth of the wakes behind a linear array of roughness element, which usually occurs in a region where their spanwise length scale is of the order of the local boundary layer thickness (e.g., Ergin and White, 2006) and (as will be shown below) the flow is governed by the BRE. We, therefore, consider an incompressible flat-plate boundary layer that is perturbed by a spanwise- periodic linear array of roughness elements at some downstream location, say $x^* = x_0^*$, where the boundary layer thickness is large compared to the roughness height, and suppose that the spanwise wavelength of the array, say $2\pi l\,\delta^*$, where l is an $O(1)$ constant, is comparable to the local value of the boundary-layer thickness $\delta^* \equiv x_0^* / \sqrt{R} = x_0^* \delta$ (or equivalently, the similarity length scale) at x_0^* where $R \equiv x_0^* U_\infty / \nu^*$ is the Reynolds number based on x_0^* and the free stream velocity U_∞, with ν^* being the kinematic viscosity and $\delta \equiv R^{-1/2} \ll 1$ being the scaled boundary layer thickness at x_0^* .

(Note that we have omitted the star superscript on U_∞ even though it denotes a dimensional quantity.) Then, in order to maximize the wake perturbation at the $O(x_0^*)$ downstream distances where (as shown in section 6 below) the streamwise ellipticity effects decay out and the motion is governed by the BRE, we require that the height of the roughness elements be as large as possible (as was done in in GSDC-1 and GSDC-2). But we now allow their streamwise length scale to be much larger than their spanwise length scale δ^* (but small compared to x_0^*) in order to minimize the recirculating flow, and thereby insure that the flow remains steady. The roughness scale flow will now match directly onto the outer BRE solution (and therefore-as noted in the introduction and as can be seen from Appendix C below-result in a much simpler asymptotic flow structure than that of the short-roughness-element flows considered in GSDC-1 and GSDC-2) if we take this longer streamwise length scale to be of the order of $\varepsilon^3 x_0^*$ where $\varepsilon \equiv R^{-1/8} = \delta^{1/4} \ll 1$. (Notice that ε is now defined differently than in GSCD-2.)

The velocity components $u(X, y_r, z)$, $v(X, y_r, z), w(X, y_r, z)$ satisfy the no-slip boundary condition

$$u(X, y_r, z) = v(X, y_r, z) = w(X, y_r, z) = 0 \qquad (2.1)$$

at the wall, where

$$y_r = \varepsilon h F(X, z) \qquad (2.2)$$

is the roughness height, $z \equiv z^* / \delta^*$, $y \equiv y^* / \delta^*$, $X \equiv (x^* - x_0^*) / \varepsilon^3 x_0^*$ and, as usual, the fluid velocity

$$\boldsymbol{v} = \{u, v, w\} \qquad (2.3)$$

and pressure p are normalized by U_∞ and $\rho^* U_\infty^2$ respectively with ρ^* being the fluid density.

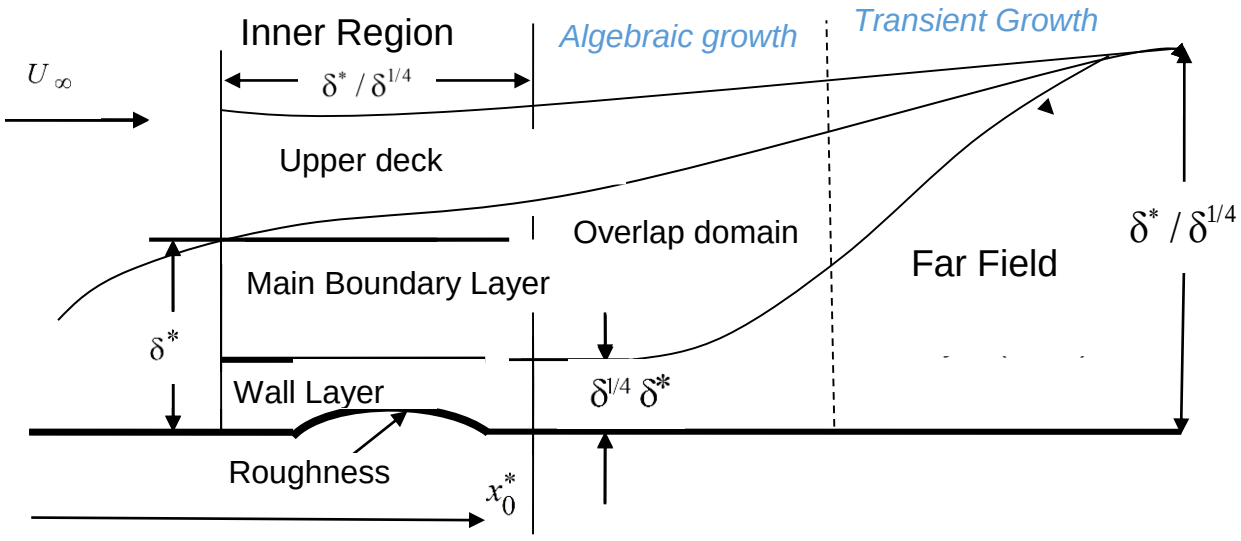

a)

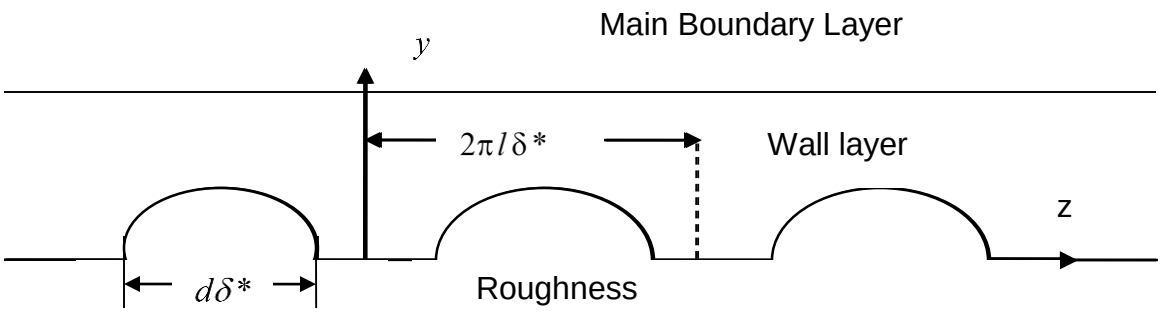

b)

Figure1. Boundary-layer flow structure, a) side view, b) cross sectional view

The scaled roughness shape function

$$F(X,z)\to 0 \ \ as\ X\to\pm\infty \tag{2.4}$$

is assumed to be more or less localized (see equations (7.1)and **Error! Reference source not found.** below) in the streamwise direction and we require that

$$p(X,y,z)\to 0,\ \text{as}\ X\to\infty \tag{2.5}$$

and

$$u(X,y,z)\to U_B(y),\ v\to\delta V_B(y)\ \ \text{as}\ X\to-\infty \tag{2.6}$$

where

$$U_B = dF_B/dy\to\lambda y+O(y^4),\ \text{as}\ y\to 0 \tag{2.7}$$

and δV_B denote the streamwise and transverse components of the Blasius velocity with the Blasius function F_B is determined by

$$\frac{d^3F_B}{dy^3}+\frac{1}{2}F_B\frac{d^2F_B}{dy^2}=0 \tag{2.8}$$

with $F_B = dF_B/dy = 0\ at\ y=0,\ dF_B/dy = 1\ at\ y=\infty$ and $\lambda\approx 0.33206$, *since* y *is equal to the Blasius variable at* $x^*=x_0^*$.

The present scaling is compared with the GSDC-1/GSCD-2 scaling in Table 1.

	Roughness length	**Roughness height**	**Roughness width**
GSDC-1, GSCD-2	δ^*	$\delta^*R^{-1/6}$	δ^*
Present paper	$\delta^*R^{1/8}$	$\delta^*R^{-1/8}$	δ^*

Table 1 Comparison of the present scaling with the GSDC-1/GSCD-2 scaling (Actual physical lengths are equal to order one constants times the scale factors.)

3. Asymptotic Structure of Near-Field Solution and Governing Equations:

3.1 Main boundary layer

As will become clear subsequently, it is appropriate to divide the boundary-layer flow into an inner streamwise region in the vicinity of the roughness elements (referred to herein as the near field of the roughness array) and an outer region (referred to here as the far field) that lies further downstream (see Figure 1a). In the main boundary layer, where $y = O(1)$ and the upstream velocity is large, the near field solution can be linearized and should, therefore, expand like

$$\{u,v,w,p\} = \{U_B,0,0,0\} + \varepsilon\{u_0(X,y), \varepsilon v_0(X,y), \varepsilon P(X)\}$$

$$+\varepsilon^2\{u_1(X,y,z), \varepsilon v_1(X,y,z),\ \varepsilon w_1(X,y,z), \varepsilon p_0^{(1)}(X,y) + \varepsilon^2 p_1(X,y,z)\} + ... \quad (3.1)$$

As will be shown below the two-dimensional $O\ \varepsilon$ terms are produced the two-dimensional distortion generated by nonlinear interactions in the wall layer (and would, therefore, be absent if the scaled roughness height were infinitesimally small). Substituting (3.1) into the incompressible Navier Stokes equations shows that these terms exhibit a triple-deck structure and are determined by the two-dimensional triple –deck equations

$$u_0 = U_B'(y)A(X), \quad v_0 = -U_B(y)\frac{dA(X)}{dX}, \quad (3.2)$$

$$\frac{d^2A(X)}{dX^2} = -\frac{1}{\pi}\int_{-\infty}^{\infty}\frac{dP(\tilde{X})/d\tilde{X}}{X-\tilde{X}}d\tilde{X} \quad (3.3)$$

with the latter equation coming flow in the upper deck. But the smaller three dimensional $O(\varepsilon^2)$ perturbations $\{u_1, v_1, w_1, P_1, p_1\}$ are now governed by the inhomogeneous linearized Euler equations

$$\frac{\partial p_0^{(1)}(X,y)}{\partial y} = U_B^2\frac{d^2A}{dX^2} \quad (3.4)$$

$$\frac{\partial u_1}{\partial X} + \frac{\partial v_1}{\partial y} + \frac{\partial w_1}{\partial z} = 0 \quad (3.5)$$

$$U_B(y)\frac{\partial u_1}{\partial X} + v_1U_B' = \frac{1}{2}\frac{dA^2}{dX}U_B^2\left[\frac{d}{dy}\left(\frac{dU_B/dy}{U_B}\right)\right] - \frac{dP}{dX} \quad (3.6)$$

and

$$U_B\frac{\partial v_1}{\partial X} = -\frac{\partial p_1}{\partial y} + U_B\frac{dU_B}{dy}\left(A\frac{d^2A}{dX^2} - \frac{dA}{dX}\frac{dA}{dX}\right) \quad (3.7)$$

where the prime on the Blasius velocity U_B denotes differentiation with respect to y.

We now introduce the decomposition

$$\{u_1, v_1, p_1\} = \{\bar{u}_1, \bar{v}_1, \bar{p}_1\} + \{u_1', v_1', p_1'\} \tag{3.8}$$

of the flow into its spanwise mean components (denoted by the over bars) and its spanwise-varying components with a zero mean and rewrite these equations in the following form

$$\frac{\partial^2 p_1'}{\partial y^2} + \frac{\partial^2 p_1'}{\partial z^2} - 2\frac{dU_B/dy}{U_B}\frac{\partial p_1'}{\partial y} = 0. \tag{3.9}$$

$$U_B(y)\frac{\partial^2 u_1'}{\partial X^2} = \left(\frac{dU_B/dy}{U_B}\right)\frac{\partial p_1'}{\partial y} \tag{3.10}$$

$$U_B\frac{\partial v_1'}{\partial X} = -\frac{\partial p_1'}{\partial y}, \quad U_B\frac{\partial w_1}{\partial X} = -\frac{\partial p_1'}{\partial z} \tag{3.11}$$

$$\bar{u}_1 = \frac{\partial \bar{\psi}}{\partial y}, \quad \bar{v}_1 = -\frac{\partial \bar{\psi}}{\partial X}, \tag{3.12}$$

$$\frac{\partial \bar{p}_1}{\partial y} = \frac{d^2}{dX^2}\left(U_B\bar{\psi}\right) + \frac{dU_B^2/dy}{2}\left[A\frac{d^2A}{dX^2} - \left(\frac{dA}{dX}\right)^2\right] \tag{3.13}$$

where we have put

$$\bar{\psi} \equiv U_B(y)\left[\left[A_1(X) - P(X)\left\{\int_0^y\left[\frac{1}{U_B^2(y)} - \frac{1}{(\lambda y)^2}\right]dy - \frac{1}{\lambda^2 y}\right\}\right]\right] + \frac{dU_B}{dy}\frac{A^2(X)}{2} \tag{3.14}$$

Notice that the present scaling is different from that in GSDC-2 and that the $O(\varepsilon^2)$ pressure is now independent of z. It, therefore, only affects the spanwise mean velocity $\bar{u}_1$ and does not contribute to the equation (3.10) for the spanwise variable velocity u_1' which causes it to differ from equation (3.3) of GSDC-2.

Equation(3.3) implies that the Fourier transforms

$$\{P(X), A(X) - A_0\} = \int_{-\infty}^{\infty}\{\tilde{P}(k), \tilde{A}(k)\}e^{ikX}dk \tag{3.15}$$

of the zeroth-order pressure and displacement perturbations $\{P(X), A(X)-A_0\}$ (where A_0 is an arbitrary constant) are related by

$$\sqrt{k^2+0^2}\,\tilde{P} = k^2\tilde{A} \tag{3.16}$$

where $\sqrt{k^2+0^2} \equiv \sqrt{k+i0}\sqrt{k-i0}$ with the branch cut for $\sqrt{k\pm i0}$ taken along the negative/ positive imaginary axis. Since the flow is assumed to be periodic in the spanwise direction, it follows from equation (3.9) that the spanwise variable pressure must possess the Fourier expansion

$$p_1'(X,y,z) = \sum_{\substack{n=-\infty \\ n\neq 0}}^{n=\infty} \pi_n(y)\tilde{P}_n^{(1)}(X)e^{inz/l} \tag{3.17}$$

in terms of the solution $\pi_n(y)$ to the unit boundary value problem

$$U_B^2(y)\frac{d}{dy}\left[\frac{1}{U_B^2(y)}\frac{d\pi_n}{dy}\right] - \left(\frac{n}{l}\right)^2 \pi_n = 0, \quad n = \pm 1, \pm 2, \ldots\ldots \tag{3.18}$$

$$\pi_n(0) = 1, \quad \pi_n(y) \to 0 \ \text{ as } y \to \infty, \tag{3.19}$$

for the nth Fourier harmonic of the main deck pressure (which is now simpler than the boundary value problem (3.9) and (3.10) of GSDC-2). The spanwise Fourier coefficients $\tilde{P}_n^{(1)}(X)$ of the limiting surface pressure distribution are given by

$$P_1(X,z) \equiv p_1'(X,0,z) = \sum_{\substack{n=-\infty \\ n\neq 0}}^{n=\infty} \tilde{P}_n^{(1)}(X)e^{inz/l}. \tag{3.20}$$

Then since $y = 0$ is a regular singular point of(3.18), it follows from (3.19) and the method of Frobenius that the solution of (3.18) behaves like

$$\pi_n(y,k) \sim 1 - \frac{1}{2}\left(\frac{n}{l}\right)^2 y^2 + \frac{b_n}{3!}y^3 + O(y^4), \quad \text{as } y \to 0 \tag{3.21}$$

where b_n is a constant. And it, then follows from(2.7),(3.2)(3.10),(3.11),(3.20) and (3.21) that

$$u_0 \to \lambda A(X), \qquad \text{as } y \to 0 \tag{3.22}$$

$$\frac{\partial^2 u_1'(X,y,z)}{\partial X^2} \to \frac{1}{\lambda y}\frac{\partial^2 P_1(X,z)}{\partial z^2}, \quad \text{as } y \to 0 \tag{3.23}$$

and

$$\frac{\partial w_1(X,y,z)}{\partial X} \to -\frac{1}{\lambda y}\frac{\partial P_1(X,z)}{\partial z}, \quad \text{as } y \to 0. \tag{3.24}$$

4. Wall Layer/ Inner:

4.1 formulation and scaling

The cross flow velocity w_1 has a critical layer singularity as $y \to 0$ which causes the expansion (3.1) to break down when

$$\hat{Y} \equiv y/\varepsilon = O(1), \tag{4.1}$$

and it is therefore necessary to obtain a new solution in this region, which brings in viscous and nonparallel flow effects (see figure 1a). Equations (3.1), (3.2), (3.12)-(3.14), (3.23) and (3.24) show that the solution in this critical layer region where the upstream velocity is small (which we refer to here as the wall layer) is nonlinear and must expand like (see Choudhari and Duck, 1996)

$$\{u,v,w,p\} = \varepsilon\{U,\varepsilon^2\breve{V},\varepsilon W,\varepsilon P(X)+\varepsilon^3 P_1(X,z)\} + \ldots\ldots \tag{4.2}$$

where $P(X)$ is the leading order spanwise invariant pressure perturbation that appears in the main deck expansion (3.1) and the spanwise variable component $P_1(X,z)$ of the lower deck pressure is related to the second order main deck pressure $p_1'(X,0,z)$ by (3.20).

The Prandtl Transformation

$$Y \equiv \hat{Y} - hF(X,z) \tag{4.3}$$

$$V \equiv \breve{V} - h(F_X U + F_z W) \tag{4.4}$$

can be used to express the leading order solution $\{U,\breve{V},W,P+\varepsilon^2 P_1\}$ in terms of the solution to the three-dimensional boundary-layer equations

$$U_X + V_Y + W_z = 0 \tag{4.5}$$

$$UU_X + VU_Y + WU_z = -dP(X)/dX + U_{YY} \tag{4.6}$$

$$UW_X + VW_Y + WW_z = -\partial P_1(X,z)/\partial z + W_{YY} \tag{4.7}$$

subject to the boundary conditions

$$U = V = W = 0 \quad \text{at } Y = 0 \tag{4.8}$$

$$U \to \lambda Y;\ V,W \to 0, \quad \text{as } x \to -\infty \tag{4.9}$$

and the matching conditions

$$U \to \lambda\left[Y + A(X) + hF(X,z)\right] - \frac{1}{\lambda Y}\frac{\partial^2 P^{\dagger}(X,z)}{\partial z^2}, \quad \text{as } Y \to \infty, \tag{4.10}$$

$$\frac{\partial^2 P^{\dagger}(X,z)}{\partial X^2} \equiv -P_1(X,z) \tag{4.11}$$

$$\frac{\partial W}{\partial X} \to -\frac{1}{\lambda Y}\frac{\partial P_1(X,z)}{\partial z} \quad \text{as } Y \to \infty \tag{4.12}$$

where we have used equations (2.7),(3.1), (3.22)-(3.24), (4.1)-(4.3), (3.22)-(3.24) to obtain the latter conditions.

It should be noted that the spanwise mean and spanwise variable components of the pressure, $P(X)$ and $P_1(X,z)$ respectively, are not externally imposed in this case but are determined as part of the viscous-inviscid interactive solution --with the novel feature being that $P_1(X,z)$ satisfies the zero displacement requirement implied by (4.10) while $P(X)$ is related to the mean boundary layer displacement $A(X)$ in the usual way by (3.3). This is different from the more conventional boundary value problem (3.19)-(3.24) of GSDC-2 which involves the single (internally determined) pressure variable P .

4.2 The numerical solution

The numerical scheme for treating (4.5)-(4.6) was an adaptation of the spectral method of Duck & Burggraf (1986). Differentiating (4.6) with respect to Y and invoking the continuity equation (4.5) yields

$$\hat{\tau}_{YY} - \lambda Y\hat{\tau}_X + \lambda W_z = \hat{\tau}U_X + U\hat{\tau}_X + V_Y\hat{\tau} + V\hat{\tau} + W_Y U_z + W\hat{\tau}_z \equiv R^{(X)}, \tag{4.13}$$

where we have written $U = \lambda Y + \mathcal{U}$ and set

$$\hat{\tau} = \mathcal{U}_Y \tag{4.14}$$

so that the hat and script variables are zero in the case of undisturbed flow and satisfy the transverse boundary conditions

$$\mathcal{U} \to \lambda\left[A(X) + hF(X,z)\right], \ \hat{\tau} \to 0 \quad \text{as } Y \to \infty, \tag{4.15}$$

$$\mathcal{U} = 0, \ \hat{\tau}_Y = dP/dX \quad \text{at } Y = 0, \tag{4.16}$$

Correspondingly we write (4.7) in the form

$$W_{YY} - \lambda Y W_X - P_z^{(1)} = \mathcal{U}W_X + VW_Y + WW_z \equiv R^{(z)}. \tag{4.17}$$

where W satisfies the obvious homogeneous boundary conditions at $Y = 0$ and $Y \to \infty$.

It is natural to use a spectral method in the spanwise direction z since the flow is periodic in that direction, but we also use a spectral method in the streamwise direction (X) and, therefore, Fourier decompose the solution in those directions to obtain

$$\{\hat{\tau}, \mathcal{U}, W, P_1, F\} = \sum_{n=-\infty}^{\infty} e^{inz/\ell} \int_{-\infty}^{\infty} \left\{\tilde{\tau}_n, \tilde{\mathcal{U}}_n, \tilde{\mathcal{W}}_n, \tilde{\mathcal{P}}_1^{(n)}, \tilde{\mathcal{F}}_n\right\} e^{ikX} dk. \tag{4.18}$$

The Fourier transforms of the momentum equations, (4.13),(4.14) and (4.17) can then be written in the following symbolic form, for each choice of k and n :

$$\tilde{\tau}_{nYY} - ik\lambda Y\tilde{\tau}_n + i\lambda\left(n/l\right)\tilde{\mathscr{W}}_n = \tilde{\mathscr{R}}_n^{(X)} \tag{4.19}$$

$$\tilde{\mathscr{W}}_{nYY} - ik\lambda Y\tilde{\mathscr{W}}_n + i\left(n/l\right)\tilde{\mathscr{P}}_n^{(1)} = \tilde{\mathscr{R}}_n^{(z)} \tag{4.20}$$

where $\tilde{\mathscr{R}}_n^{(X)}$ and $\tilde{\mathscr{R}}_n^{(z)}$ represent the double spectral decompositions of $R^{(X)}$ and $R^{(z)}$ respectively and it follows from(4.16), (4.15) and (3.16) that $\tilde{\tau}_n$ satisfies the following conditions

$$\int_0^\infty \tilde{\tau}_n dY = \lambda\left(h\,\mathrm{F}_n + \delta_{n,0}\tilde{P}\sqrt{k^2+0^2}\,/\,k^2\right) \tag{4.21}$$

$$\tilde{\tau}_{nY} = ik\delta_{n,0}\tilde{P},\ \text{for}\ \ Y=0 \tag{4.22}$$

where $\delta_{i,j}$ denotes the Kronecker Delta and $\tilde{P}\left(k\right)$ is defined by (3.15). Note that some of the integration contours in(4.18) have to be deformed in the manner described in section 5 below because some of the quantities on the left hand side become unbounded as $X\to\infty$ and that (4.15) implies that $\tilde{\tau}_n \to 0$ as $Y\to\infty$.

Second-order finite differencing was employed in the Y -direction in conjunction with a non-uniform grid that concentrated grid points close to $Y=0$ and also extended the grid to relatively large values in Y in order to capture the algebraic decay as $Y\to\infty$. Generally we used the transformation $Y = Y_1/\left(1-Y_1\right)$ with a uniform grid in Y_1.

In Duck& Burggraf (1986) the nonlinear contributions to the momentum equations were evaluated using a pseudo-spectral approach, using fast Fourier transform (FFT) algorithms to switch between physical and spectral space (taking advantage of the associated speedup in computation). However, although an FFT procedure was implemented, a convolution procedure to evaluate the nonlinear terms was preferred. The reason for this was that the far downstream $\left(X\to\infty\right)$ behavior of the solution is of particular interest in this study. While some of the integrals in (4.18) have to be interpreted as contour integrals because their integrands become singular as $k\to 0$ only integrable singularities appeared in the integrals used in the computations and the integrations could be carried out along the real axis. But this still required the use of an extremely fine spectral resolution in k -space in order to perform accurate computations of the downstream asymptotes. Consequently, a non-uniform grid was again taken, specifically, $k = k_1(1-exp(-k_1^2))$, which had the effect of concentrating points close to $k=0$ when a uniform grid in k_1 space was taken. Needless to say, extensive numerical grid studies were undertaken in order to confirm the accuracy/integrity of our computations. The Hermitian property of the transform variables was also exploited. The downside is that this renders the overall system inconvenient for FFT procedures. An iterative approach which first considered all k points and then all n terms in turn, was repeatedly used , until the required level of tolerance had been achieved.

5. Asymptotic structure of near field solution at large downstream distances

When $X \to \infty$, the second order surface pressure $P_1(X,z)$ is expected to decay like $\left(\ln X^{1/3}\right)^{\beta} / X^{\alpha}$ (see GSDC-1 and GSDC-2) which means that the first-order displacement must grow like $\left(\ln X^{1/3}\right)^{\beta} / X^{(\alpha_0 - 1)}$ in order to balance the nonlinear terms (see analysis in Appendix A) , i.e.,

$$A(X) - A_0 \sim \hat{A}\left[\ln(X/\lambda)^{1/3}\right]^{\beta} / (X/\lambda)^{(\alpha_0 - 1)} \tag{5.1}$$

and

$$P_1(X,z) \sim \hat{p}(0,z)\frac{\left[\ln(X/\lambda)^{1/3}\right]^{\beta}}{(X/\lambda)^{\alpha}} \text{ as } X \to \infty. \tag{5.2}$$

where $\hat{A}, \alpha_0, \alpha, \beta$ are constants (see GSDC-1 and GSDC-2) and we have introduced the $\hat{p}(0,z)$ term in anticipation of the $\hat{p}(0,z)$ term that appears in the downstream asymptote of the main-deck solution. It then follows from (3.17) and (3.20) that the spanwise-variable pressure in the main deck has the downstream asymptote given by

$$p_1'(X,y,z) \sim \hat{p}(y,z)\left[\ln(X/\lambda)^{1/3}\right]^{\beta} / (X/\lambda)^{\alpha} \quad \text{as } X \to \infty, \tag{5.3}$$

where

$$\hat{p}\ (y,z) \equiv \sum_{\substack{n=-\infty \\ n\neq 0}}^{n=\infty} \pi_n(y)\tilde{A}_n e^{inz/l}. \tag{5.4}$$

Substituting the expansion (3.21) for the near wall behavior of the unit solutions π_n into (5.4) yields

$$\hat{p}(y,z) \sim \sum_{\substack{n=-\infty \\ n\neq 0}}^{n=\infty}\left[1 - \frac{1}{2}\left(\frac{n}{l}\right)^2 y^2 + O\left(y^3\right)\right]\tilde{A}_n e^{inz/l} \tag{5.5}$$

as $y \to 0$.

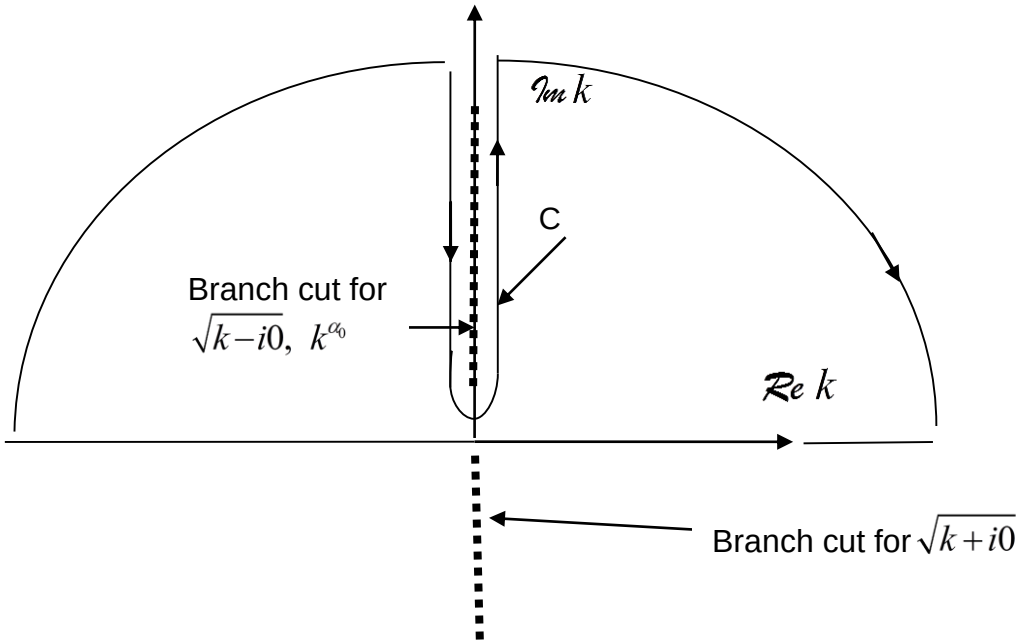

Figure 2 Integration contour for (5.6) with $X>0$

Deforming the integral (3.15) onto the contour C shown in figure 2 and inserting the pressure-displacement relation (3.16) yields

$$\{P(X),A(X)\}=-\oint_C\left\{\varsigma^2/\sqrt{\varsigma^2+0},1\right\}\tilde{A}(\varsigma)e^{iX\varsigma}d\varsigma \tag{5.6}$$

It then follows from equations 6.1.4 and 6.1.17 of Abramowitz and Stegun (1965) that

$$\int_C e^{iX\varsigma}\varsigma^{\nu}d\varsigma=\frac{\left(e^{i\pi\nu/2}-e^{-3i\pi\nu/2}\right)\Gamma(\nu+1)}{iX^{(\nu+1)}} \tag{5.7}$$

and

$$\int_C e^{iX\varsigma}\frac{\varsigma^{\nu}}{\sqrt{\varsigma+i0}\sqrt{\varsigma-i0}}d\varsigma=\frac{\left(e^{i\pi\nu/2}+e^{-3i\pi\nu/2}\right)\Gamma(\nu)}{X^{\nu}} \tag{5.8}$$

where $\nu<1$ denotes a non-integer constant, the branch cut of ς^{ν} is taken along the positive imaginary axis and $\Gamma(\nu)$ denotes the Gamma function. (This also follows from (3.15)and Table I of Lighthill, 1964.)

Then $A(X)$ will exhibit the asymptotic behavior (5.1) when α_0 is not an integer and $\beta=0$ if $\tilde{A}(k)$ behaves like

$$\tilde{A}(k) \to \frac{a e^{i\pi(\alpha_0-2)/2}(k\lambda)^{\alpha_0}}{\lambda k^2} \quad \text{as} \quad k \to 0 \tag{5.9}$$

where a is related to the constant $\hat{A}$ in (5.1) by

$$\hat{A} = -2a \sin\pi(\alpha_0 - 2)\Gamma(\alpha_0 - 1) \tag{5.10}$$

In which case (5.8) would show that

$$\tilde{P}(k) \to \frac{a e^{i\pi(\alpha_0-2)/2}(k\lambda)^{\alpha_0}}{\lambda\sqrt{k+i0}\sqrt{k-i0}} \quad \text{as} \quad k \to 0 \tag{5.11}$$

and, therefore, that the leading order spanwise invariant pressure perturbation in the main deck has the downstream asymptote

$$P(X) \sim \hat{P}/(X/\lambda)^{\alpha_0}, \quad X \to \infty \tag{5.12}$$

where

$$\hat{P} \equiv \frac{-2a\cos\pi(\alpha_0 - 2)\Gamma(\alpha_0)}{\lambda} \tag{5.13}$$

Aside from its scaling, the downstream flow is similar to that in GSDC-2, which shows that it is completely linear when α is sufficiently large and that solutions only exist when $\alpha = n/3$, for $n = 1, 2, \ldots$. However, GSDC-1 also showed that the wall layer equations can become nonlinear when α is decreased to 4/3 with $\beta = 0$. And since our interest here is in maximizing the strength of the downstream we now choose α=4/3, $\beta = 0$ and set $\alpha_0 = 2/3$ in order to match the resulting main deck solutions to the similarity wall layer solution. (It will show in section 7 below that this scaling is consistent with the asymptotic behavior of the numerical nearfield solutions for fairly generic roughness shapes.)

The main-deck equations (3.2) and (3.10)-(3.14) then possess the exact solution

$$u_0 = U_B'(y)\hat{A}(X/\lambda)^{1/3}, \tag{5.14}$$

$$v_0 = -U_B(y)\hat{A}/\left[\lambda 3(X/\lambda)^{2/3}\right], \tag{5.15}$$

$$P(X) = \hat{P}/(X/\lambda)^{2/3} \tag{5.16}$$

$$\bar{p}_1(X, y) = -\frac{2\hat{A}}{(3\lambda)^2(X/\lambda)^{5/3}}\int_0^y U_B^2(y)\,dy \tag{5.17}$$

$$p_1'(X, y, z) = \hat{p}(y, z)/(X/\lambda)^{4/3}, \tag{5.18}$$

$$u_1'(X, y, z) = -\frac{(3\lambda)^2(X/\lambda)^{2/3}}{2}\frac{U_B'(y)}{U_B^2(y)}\frac{\partial}{\partial y}\hat{p}(y, z), \tag{5.19}$$

$$v_1'(X,y,z)=\frac{3\lambda}{(X/\lambda)^{1/3}U_B(y)}\frac{\partial\hat{p}(y,z)}{\partial y}, \tag{5.20}$$

$$w_1(X,y,z)=\frac{3\lambda}{(X/\lambda)^{1/3}U_B(y)}\frac{\partial\hat{p}(y,z)}{\partial z}, \tag{5.21}$$

which can be regarded as the leading-order terms in an asymptotic expansion of the solution to the complete boundary-value problem. It then follows from (2.7), (3.17), (3.21), (5.1)and (5.5) that

$$u_0\sim\lambda\hat{A}X^{1/3}, \tag{5.22}$$

$$w_1(X,y,z)\sim\frac{3}{(X/\lambda)^{1/3}y}\frac{\partial\hat{p}(0,z)}{\partial z}\ , \tag{5.23}$$

$$u_1'(X,y,z)\sim-\frac{3^2\lambda(X/\lambda)^{2/3}}{2y}\frac{\partial^2\hat{p}(0,z)}{\partial z^2}, \tag{5.24}$$

as $y\to 0$.

Equation (5.16) implies that the spanwise mean pressure must drop out of the wall layer equations (4.5)-(4.12) when $X\to\infty$ and the resulting equations then an exact similarity solution ,which corresponds to setting $\lambda=4/3$ in the general (4.12) of GSDC-2 and is therefore of the form

$$W=(X/\lambda)^{-2/3}\tilde{W}(\eta,z),\ \ U=\lambda(X/\lambda)^{1/3}\tilde{U}(\eta,z),\ \ \ V=(X/\lambda)^{-1/3}\tilde{V}(\eta,z), \tag{5.25}$$

with the similarity variable η given by

$$\eta\equiv Y/(X/\lambda)^{1/3}. \tag{5.26}$$

and $\tilde{U},\tilde{V},\tilde{W}$ are determined by

$$\frac{1}{3}(\tilde{U}-\eta\tilde{U}_\eta)+\tilde{V}_\eta+\tilde{W}_z=0, \tag{5.27}$$

$$-\frac{1}{3}\tilde{U}(2\tilde{W}+\eta\tilde{W}_\eta)+\tilde{V}\tilde{W}_\eta+\tilde{W}\tilde{W}_z=-\frac{\partial\hat{p}(0,z)}{\partial z}+\tilde{W}_{\eta\eta}, \tag{5.28}$$

$$\frac{1}{3}\tilde{U}(\tilde{U}-\eta\tilde{U}_\eta)+\tilde{V}\tilde{U}_\eta+\tilde{W}\tilde{U}_z=\tilde{U}_{\eta\eta}, \tag{5.29}$$

subject to the no-slip/ impermeability boundary conditions

$$\tilde{U}(0,z)=\tilde{V}(0,z)=\tilde{W}(0,z)=0. \tag{5.30}$$

Equations (3.1), (4.2) and (5.22)- (5.25) show that these solutions will match onto the near-wall behavior of the main boundary-layer solution if we require that

$$\tilde{W}(\eta,z)\to\frac{3}{\eta}\frac{\partial\hat{p}(0,z)}{\partial z}, \tag{5.31}$$

$$\tilde{U}(\eta,z)\to\eta+\hat{A}-\frac{3^2}{2\eta}\frac{\partial^2\hat{p}(0,z)}{\partial z^2}, \tag{5.32}$$

as $\eta\to\infty$.

Equations (5.27)-(5.29) can be simplified by introducing the variable

$$\tilde{\mathcal{V}}\equiv\tilde{V}-\frac{\eta}{3}\tilde{U} \tag{5.33}$$

to obtain

$$\frac{2}{3}\tilde{U}+\tilde{\mathcal{V}}_\eta+\tilde{W}_z=0, \tag{5.34}$$

$$-\frac{2}{3}\tilde{U}\tilde{W}+\tilde{\mathcal{V}}\tilde{W}_\eta+\tilde{W}\tilde{W}_z=-\frac{\partial\hat{p}(0,z)}{\partial z}+\tilde{W}_{\eta\eta}, \tag{5.35}$$

$$\frac{1}{3}\tilde{U}^2+\tilde{\mathcal{V}}\tilde{U}_\eta+\tilde{W}\tilde{U}_z=\tilde{U}_{\eta\eta}, \tag{5.36}$$

And it now follows from (5.32)-(5.34) that

$$\tilde{\mathcal{V}}_\eta\to-\frac{2}{3}\left(\eta+\hat{A}\right)+O\left(\eta^{-2}\right),\ \text{as}\ \eta\to\infty \tag{5.37}$$

while equations (5.30), (5.34) and (5.33) show that

$$\tilde{\mathcal{V}}=\tilde{\mathcal{V}}_\eta=0\ \text{ at}\ \eta=0 \tag{5.38}$$

Using (5.34) to eliminate $\tilde{U}$ in (5.35) yields

$$\left(\tilde{\mathcal{V}}\tilde{W}\right)_\eta+\left(\tilde{W}^2\right)_z=-\frac{\partial\hat{p}(0,z)}{\partial z}+\tilde{W}_{\eta\eta}, \tag{5.39}$$

The system (5.34)-(5.38) can be further reduced to a set of two equations in the two independent variables $\tilde{W}$ and $\tilde{\mathcal{V}}$ by using (5.34) together with this result to eliminate $\tilde{U}$ in (5.36) to obtain

$$-\frac{3}{2}\left(\tilde{\mathcal{V}}_\eta+\tilde{W}_z\right)^2+\left[\tilde{\mathcal{V}}\left(\tilde{\mathcal{V}}_\eta+\tilde{W}_z\right)\right]_\eta-\left(\tilde{W}\tilde{W}_z+\tilde{\mathcal{V}}\tilde{W}_\eta\right)_z=\frac{\partial^2\hat{p}(0,z)}{\partial z^2}+\tilde{\mathcal{V}}_{\eta\eta\eta} \tag{5.40}$$

However, it turns out to be more convenient for numerical purposes to solve system (5.34) ,(5.36), and (5.39) rather than (5.39)and (5.40) and the former were, therefore, used for the computations described in section 7 of this paper. It is easy to construct an analytical solution to the boundary value problem obtained by linearizing these equations about $\tilde{U}=\eta$ and $\tilde{\mathcal{V}}=-\frac{1}{3}\eta^2$. We obtain the solution to the nonlinear problem by iterating about the linear

result since the numerical computations show that $\tilde{U}-\eta$ is quite small and, hence, the linear solution is expected to be a fairly accurate approximation to the solution to the nonlinear problem. The details are given in Appendix A and the exact solution to the linearized problem is given by equations (A.6),(A.10) and (A.11) with $F=G=0$.

The exact homogeneous solution (5.14)-(5.21) and (5.25) does not satisfy the complete boundary value problem (4.5)-(4.12), but the asymptotic solution to this problem can be found by treating this solution as the lowest order term in an asymptotic expansion in inverse powers of $X^{1/3}$. For example, the spanwise variable pressure is expected to expand like

$$p_1'(X,y,z)=\hat{p}(y,z)/(X/\lambda)^{4/3}+\hat{p}_1(y,z)/(X/\lambda)^{5/3}+\ldots\ldots, \qquad (5.41)$$

while the wall layer solution should have an expansion of the form

$$W=(X/\lambda)^{-2/3}\tilde{W}(\eta,z)+(X/\lambda)^{-1}\tilde{W}_1(\eta,z)+\ldots., \quad U=\lambda\Big[(X/\lambda)^{1/3}\tilde{U}(\eta,z)+$$

$$\tilde{U}_1(\eta,z)+\ldots\Big], \quad V=(X/\lambda)^{-1/3}\tilde{V}(\eta,z)+(X/\lambda)^{-2/3}\tilde{V}_1(\eta,z)+\ldots., \qquad (5.42)$$

The second-order terms are important because, as will be shown in section 7 below (see figures 8 and 11), $\hat{p}_1(0,z)$ turns out to be much larger than $\hat{p}(0,z)$. This implies (among other things) that the leading-order terms only become dominant at very large positive values of X (see figure 7 below).

6. Far field solution and matching with the near field (see Figure 1a):

Inserting equations (5.22) and (5.24) into the expansion (3.1) shows that the near-field solution breaks down when $X^{1/3}\varepsilon=O(1)$ because the $O(\varepsilon)$ and $O(\varepsilon^2)$ terms then become of the same order of magnitude. It is, therefore, necessary to obtain a new expansion in the far field (or outer region) where

$$x\equiv x^*/x_0^*=\varepsilon^3X+1, \qquad (6.1)$$

is $O(1)$. The flow in this (outer) region now has an expansion of the form

$$\{u,v,w,p\}=\{\tilde{u}(x,y,z),\delta\tilde{v}(x,y,z),\delta\tilde{w}(x,y,z),\delta\,\tilde{p}_0(x)+\delta^2\tilde{p}(x,y,z)\}$$

$$+\varepsilon\{\tilde{u}_1(x,y,z),\delta\tilde{v}_1(x,y,z),\delta\tilde{w}_1(x,y,z),\delta\,\tilde{p}^{(1)}(x)+\delta^2\tilde{p}_1(x,y,z)\}+\ldots\ldots \qquad (6.2)$$

with $\delta\equiv R^{-1/2}=\varepsilon^4$ and the lowest order solution $\{\tilde{u},\tilde{v},\tilde{w},\tilde{p}\}$ being determined by the full nonlinear BRE

$$\tilde{u}_x+\tilde{v}_y+\tilde{w}_z=0, \qquad (6.3)$$

$$\tilde{u}\tilde{u}_x+\tilde{v}\tilde{u}_y+\tilde{w}\tilde{u}_z=\tilde{u}_{yy}+\tilde{u}_{zz}, \qquad (6.4)$$

$$\tilde{u}\tilde{v}_x+\tilde{v}\tilde{v}_y+\tilde{w}\tilde{v}_z=-\tilde{p}_y+\tilde{v}_{yy}+\tilde{v}_{zz}, \qquad (6.5)$$

$$\tilde{u}\tilde{w}_x + \tilde{v}\tilde{w}_y + \tilde{w}\tilde{w}_z = -\tilde{p}_z + \tilde{W}_{yy} + \tilde{W}_{zz}, \tag{6.6}$$

indicating that spanwise ellipticity effects must be preserved in this region. The leading-order flow variables must satisfy the wall-normal boundary conditions

$$\tilde{u},\tilde{v},\tilde{w} = 0; \text{ for } y = 0; \ \tilde{u} \to 1,\tilde{w},\tilde{p} \to 0, \text{ as } y \to \infty, \tag{6.7}$$

along with appropriate upstream matching conditions.

6.1 Main boundary Layer:

It can be verified by direct substitution that equations (6.3) to (6.6) permit a solution with an inner (i.e., upstream) limit of the form

$$\tilde{u} = U_B(y) + (x-1)^{1/3}\tilde{u}^{(0)}(y) + (x-1)^{2/3}\tilde{u}^{(1)}(y,z) + ... \tag{6.8}$$

$$\begin{Bmatrix} \tilde{v} \\ \tilde{w} \end{Bmatrix} = \begin{Bmatrix} \delta V_B(y) \\ 0 \end{Bmatrix} + \frac{1}{(x-1)^{2/3}} \begin{Bmatrix} \tilde{v}^{(0)}(y) \\ 0 \end{Bmatrix} + \frac{1}{(x-1)^{1/3}} \begin{Bmatrix} \tilde{v}^{(1)}(y,z) \\ \tilde{w}^{(1)}(y,z) \end{Bmatrix} + ... \tag{6.9}$$

$$\tilde{p}(x,y,z) = P^{(1)}(y)/(x-1)^{5/3} + \tilde{p}^{(1)}(y,z)/(x-1)^{4/3} + ..., \tag{6.10}$$

as $x \to 1$ with $y = O(1)$, where the coefficients $\tilde{u}^{(1)}, \tilde{V}^{(1)}, \tilde{w}^{(1)}, \tilde{p}^{(1)}$ satisfy the linear equations

$$\frac{2}{3}\tilde{u}^{(1)} + \tilde{v}_y^{(1)} + \tilde{w}_z^{(1)} = 0, \tag{6.11}$$

$$\frac{2}{3}U_B(y)\tilde{u}^{(1)} + \tilde{v}^{(1)}U_B'(y) = 0, \tag{6.12}$$

$$-\frac{1}{3}U_B(y)\begin{Bmatrix} \tilde{v}^{(1)} \\ \tilde{w}^{(1)} \end{Bmatrix} = -\begin{Bmatrix} \tilde{p}_y^{(1)} \\ \tilde{p}_z^{(1)} \end{Bmatrix}. \tag{6.13}$$

Eliminating $\tilde{u}^{(1)}, \tilde{V}^{(1)}, \tilde{w}^{(1)}$ between (6.11)-(6.13) shows that $\tilde{p}^{(1)}$ satisfies

$$\frac{\partial^2 \tilde{p}^{(1)}}{\partial y^2} + \frac{\partial^2 \tilde{p}^{(1)}}{\partial z^2} - 2\frac{U_B'}{U_B}\frac{\partial \tilde{p}^{(1)}}{\partial y} = 0, \tag{6.14}$$

6.2 Matching

It now follows from(6.1) and, (6.8)-(6.10) that the inner expansion of the outer solution as $x \to 1$ is

$$\tilde{u} \sim U_B(y) + \varepsilon\, X^{1/3}\tilde{u}^{(0)}(y) + \varepsilon^2 X^{2/3}\tilde{u}^{(1)}(y,z) + ..., \tag{6.15}$$

$$\delta\begin{Bmatrix} \tilde{v} \\ \tilde{w} \end{Bmatrix} \sim \begin{Bmatrix} \delta V_B(y) \\ 0 \end{Bmatrix} + \varepsilon^2 \frac{1}{X^{2/3}} \begin{Bmatrix} \tilde{v}^{(0)}(y) \\ 0 \end{Bmatrix} + \varepsilon^3 \frac{1}{X^{1/3}} \begin{Bmatrix} \tilde{v}^{(1)}(y,z) \\ \tilde{w}^{(1)}(y,z) \end{Bmatrix} + ..., \tag{6.16}$$

$$\delta^2\,\tilde{p} \sim \varepsilon^3 \frac{P^{(1)}(y)}{X^{5/3}} + \varepsilon^4 \frac{\tilde{p}^{(1)}(y,z)}{X^{4/3}} \quad +.... \tag{6.17}$$

Substituting (6.12) and (6.13) into the above confirms that the result will match onto the outer expansion (5.14)-(5.21) of the near field solution (3.1) if

$$\tilde{u}^{(0)}(y) = U_B'(y)\hat{A}/\lambda^{1/3}, \tag{6.18}$$

$$\tilde{v}^{(0)}(\hat{y}) = -U_B(y)\hat{A}/\lambda^{1/3}3, \tag{6.19}$$

$$P^{(1)}(y) = -\frac{2\hat{A}}{3^2\lambda^{1/3}}\int_0^y U_B^2(y)\,dy \tag{6.20}$$

and

$$\tilde{p}^{(1)}(y,z) = \lambda^{4/3}\hat{p}(y,z), \tag{6.21}$$

where $\hat{p}(y,z)$ is given by (5.4), since equations (3.9), (5.18), (6.10)and (6.14) show that that the spanwise variable pressure $\tilde{p}^{(1)}(y,z)$ satisfies the same equation and boundary conditions as the near field pressure $\hat{p}$.

However, the solutions (6.11)-(6.13) do not satisfy the correct wall boundary condition since equations(3.21), (5.5)-(6.13) and (6.21) show that $\tilde{w}^{(1)} \to \infty$ as $y \to 0$. In fact it follows from (5.5)and (6.21) that

$$\tilde{p}^{(1)} \sim \tilde{p}^{(1)}(0,z) + \frac{y^2}{2}\frac{\partial^2}{\partial z^2}\tilde{p}^{(1)}(0,z) + ... \tag{6.22}$$

when $\tilde{p}^{(1)}(0,z)$ is non-zero, which implies that

$$\tilde{w}^{(1)} \sim \frac{3}{\lambda y}\frac{\partial \tilde{p}^{(1)}(0,z)}{\partial z}, \tag{6.23}$$

$$\tilde{v}^{(1)} \sim \frac{3}{\lambda}\frac{\partial^2}{\partial z^2}\tilde{p}^{(1)}(0,z), \tag{6.24}$$

$$\tilde{u}^{(1)} \sim \frac{-3^2}{2y\lambda}\frac{\partial^2}{\partial z^2}\tilde{p}^{(1)}(0,z) \tag{6.25}$$

as $y \to 0$.

6.3 Wall Layer

The lowest-order terms in the expansion (6.8) to (6.10) satisfy inviscid equations and, therefore, clearly cannot satisfy the no-slip condition at the wall. This means that it is necessary to derive solutions in a viscous wall layer near the surface of the plate. The viscous and inertial terms will be of the same order of magnitude in the BRE when $y/(x-1) \sim 1/y^2$, which suggests introducing the similarity variable

$$\eta = \frac{\lambda^{1/3} y}{(x-1)^{1/3}} \tag{6.26}$$

It then follows from the spanwise momentum equation (6.6) and the expansions (6.8) to (6.10) that the viscous and inertial terms will balance the spanwise pressure gradient if $\tilde{w}$ is of the form

$$\tilde{w} = \lambda^{2/3}(x-1)^{-2/3}\tilde{W}(\eta, z) \tag{6.27}$$

while the continuity and the streamwise momentum equations (6.3) and (6.4) then imply that $\tilde{u}$ and $\tilde{v}$ must be of the form

$$\tilde{u} = \lambda^{2/3}(x-1)^{1/3}\tilde{U}(\hat{\eta}, z) \tag{6.28}$$

and

$$\hat{v} = (x-1)^{-1/3}\lambda^{1/3}\tilde{V}(\eta, z) \tag{6.29}$$

Inserting (6.27) and (6.28) into the BRE (6.3)-(6.6) shows that $\tilde{U}(\eta, z)$, $\tilde{V}(\eta, z)$, $\tilde{W}(\eta, z)$ must satisfy (5.27) to (5.29) subject to the boundary conditions (5.30)-(5.32) but with η now given by (6.26) instead of by (5.26). The outer (or far wake) wall layer solution is therefore identical to the asymptotic wall layer of section 5--in fact equations (2.4), (4.1), (4.3) and (6.26) show that it is merely the continuation of that layer into the outer region. These results imply that there is an overlap domain in which the far downstream asymptotic form of the near field solution matches onto the inner expansion of the BRE solution that satisfies (6.8) to (6.10) as $x \to 1$ in the main part of the boundary layer.

Since the BRE are parabolic in the streamwise direction, equations (6.8)-(6.10) and (6.26)-(6.29) provide appropriate upstream boundary conditions for those equations in their appropriate range of validity. These conditions are best implemented numerically by solving the BRE system (6.3)-(6.7) subject to the uniformly valid composite upstream boundary conditions (Van Dyke, 1975, pp. 94-96)

$$\tilde{p}(x, y, z) \to -\frac{2\hat{A}}{3^2\lambda^{1/3}(x-1)^{5/3}}\int_0^y U_B^2(y)\,dy + \frac{\lambda^{4/3}\hat{p}(y, z)}{(x-1)^{4/3}} \tag{6.30}$$

$$\tilde{u} \to U_B(y) - \lambda\hat{y} + (x-1)^{1/3}\left\{\left[U_B'(y) - \lambda\right]\lambda^{1/3}\hat{A} + (x-1)^{1/3}\left[\tilde{u}^{(1)}(y, z) + \right.\right. \tag{6.31}$$

$$\left.\left.\frac{3^2\lambda^{1/3}}{2}\left[\left[\hat{p}_{zz}(0, z)/y + \frac{1}{2}\hat{p}_{yyy}(0, z)(1 - \tanh\eta)\right]\right] + \lambda^{2/3}\tilde{U}(\eta, z)\right]\right\}$$

$$\tilde{v}(\mathrm{x},y,z)\to V_B(y)-\frac{1}{(x-1)^{1/3}}\left\{\frac{\left[U_B(y)-\lambda y\right]\lambda^{1/3}\hat{A}}{(x-1)^{1/3}\,3}-\tilde{v}^{(1)}(y,z)+3\lambda^{1/3}\frac{\partial^2}{\partial z^2}\hat{p}(0,z)\right.$$

$$\left.-\lambda^{1/3}\tilde{V}(\eta,z)\right\} \qquad (6.32)$$

$$\tilde{w}(x,y,z)\to\frac{1}{(x-1)^{2/3}}\left\{(x-1)^{1/3}\left[\tilde{w}^{(1)}(y,z)-\frac{3\lambda^{1/3}}{y}\frac{\partial\hat{p}(0,z)}{\partial z}\right]+\lambda^{2/3}\tilde{W}(\eta,z)\right\}, \qquad (6.33)$$

as $x\to 1$. The various terms in these equations can be obtained from (6.12), (6.13) with $\tilde{U}(\eta,z)$, $\tilde{V}(\eta,z)$,$\tilde{W}(\eta,z)$ being obtained by solving the boundary value problem (5.34)-(5.38) and (5.30)-(5.32) with η now given by (6.26). We have included the higher order term proportional to $\hat{p}_{yyy}(0,z)$ in the wall layer solution in order to insure that $\tilde{u}=0$ at $y=0$ when $x-1$ is reasonably large. The $(1-\tanh\eta)$ factor eliminates the contribution from the main boundary layer.

The $O(\varepsilon)$ terms in the expansion (6.2) satisfy linearized equations and match onto the second terms in the expansions (5.41)and(5.42) in the limit as $x\to 1$. The relative size of the first two terms in (6.2) is therefore expected to be $O\left(\varepsilon\max\left\{\hat{p}_1(0,z)/\,\hat{p}(0,z)\right\}\right)$ when $x-1$ is sufficiently small.

6.4 Numerical solution

The non-linear BRE (6.3)-(6.7) are parabolic in the streamwise x-direction and can, therefore be solved by a marching algorithm. The wall-normal (y-direction) and spanwise (z- direction) derivatives were discretized by a centered finite-difference scheme that was second order in the y-direction and fourth order in the z-direction. A backward finite difference scheme of first order of accuracy is utilized in the streamwise x-direction. The pressure and velocity fields were computed on separate grids that were staggered in the wall-normal y-direction, in order to avoid pressure-velocity decoupling that could contaminate the solution by generating spurious waves (Harlow & Welch, 1965). No wall boundary condition was required for the pressure component, while the velocity components were set to zero there (no-slip condition). Due to the spanwise symmetry of the flow with respect to the center of the roughness elements, we were able to use symmetry conditions for the pressure, streamwise and wall-normal components of velocity, and anti-symmetry condition for the spanwise component of velocity to compute the numerical solution on half of the spanwise length (representing the distance between the centers of two roughness elements). A relaxation algorithm, with pseudo-time derivatives added to the equations was used to solve the resulting system of nonlinear discretized equations (Jameson, 1991), which were then converged to the final solution via a Runge-Kutta method with appropriate preconditioning applied to the first equation (6.3) to avoid stability issues.

The initial/upstream conditions for this solution are given by the uniformly valid composite

solution (6.30)-(6.33), with the similarity variables $\tilde{U}(\eta,z)$, $\tilde{V}(\eta,z)$,$\tilde{W}(\eta,z)$ obtained by using the iterative procedure described in Appendix A to solve the boundary value problem (5.34)-(5.38) and (5.30)-(5.32). Gauss quadrature was used to approximate all integrals in equations (A.12)-(A.20) and a relaxation method was used to solve (A.14) for (Young, D. M., 1954), $\tilde{U}(\eta,z)$, in order to avoid approximating the triple integrals in (A.10),which are prone to errors. Second order finite difference schemes were used to approximate all first order derivatives in equations (A.12) and (A.14) . Only three or four iterations, depending on the roughness element height, were needed to converge the similarity solution.

7. Results and Discussion

The previous sections provide a theoretical description of the near field, intermediate field and far field flow over a spanwise periodic array of elongated roughness elements with a fundamental spanwise spacing of the order of the boundary-layer thickness. The numerical behavior of these flows will be discussed in this section and all computations will be based on the smooth shape function

$$F(X,z)=\frac{\hat{F}(z)}{1+\left(X/d_0\right)^2} \tag{7.1}$$

where $\hat{F}(z)$ is taken to be the compact infinitely differentiable function

$$\hat{F}(z)=\begin{cases}\exp\left\{-\dfrac{(z-\pi l)^2}{d^2}\left[\kappa^2+\dfrac{d^2}{d^2-(z-\pi l)^2}\right]\right\}, & \text{for } (z-\pi l)^2<d^2\\ 0, & \text{for } (z-\pi l)^2>d^2\end{cases} \tag{7.2}$$

with $d<\pi l$. The coefficients in its Fourier expansion

$$\hat{F}(z)\equiv\sum_{n=-\infty}^{n=\infty}B_n e^{inz/l} \tag{7.3}$$

are then given by

$$B_n=\frac{1}{2\pi l}\int_0^{2\pi l}e^{-inz/l}\hat{F}(z)dz=De^{-in\pi}\int_0^1\cos(D\pi n\varsigma)\exp\left[-\varsigma^2\left(\kappa^2+\frac{1}{1-\varsigma^2}\right)\right]d\varsigma \tag{7.4}$$

where

$$D\equiv d/\pi l<1, \tag{7.5}$$

The compact infinitely differentiable shape function

will also be discussed. These roughness shapes are amenable to future experiments which we hope will be inspired by this analysis.

Figure 3 is a plot of $\hat{F}(z)$ vs. $(z-\pi l)/d$ for $D=1/2$.

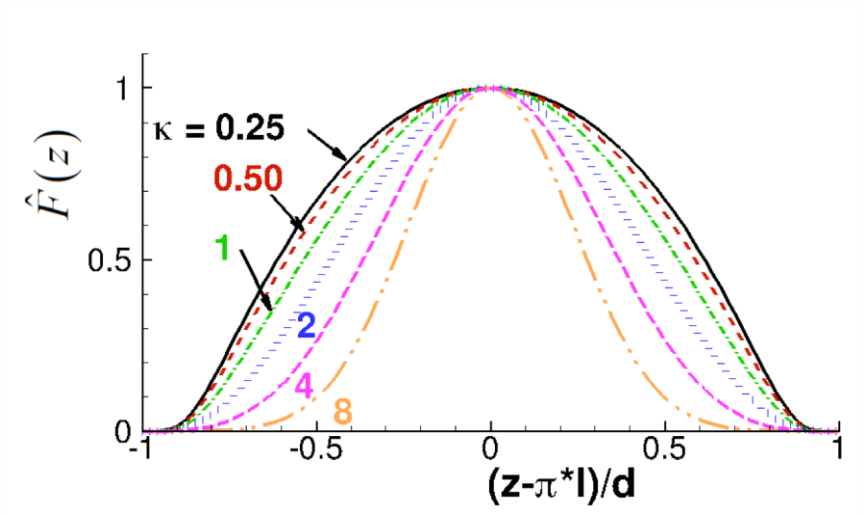

Figure 3 Spanwise shape function $\hat{F}(z)$ vs. $(z-\pi l)/d$ for $D \equiv d/\pi l = 1/2$

The roughness elements will have a circular planform when $R = 3^8 = 6{,}561$ for a roughness array corresponding to the compact shape function **Error! Reference source not found.**with $d_0 = 3d$. The present elongated-roughness scaling is therefore an attractive alternative to the short equi-dimensional planform scaling in Appendix C even for the circular shapes since the latter leads to a considerably more complicated analysis than the former.

7.1 The near field solution

Since the near field problem has a somewhat novel asymptotic structure, it seems appropriate to plot some typical results for the quantities usually calculated in triple-deck papers. The wall shear parameter λ can be scaled out of the near field triple-deck problem in the usual way and it follows from (4.5)-(4.12) and (7.2) that the scaled wall pressure $P^{(1)}(X,z)/\lambda^3$ and scaled wall shear U_Y/λ can only depend on the scaled roughness shape parameters $\lambda^{3/4}h$, l, $\lambda^{5/4}d_0$, $D \equiv d/\pi l$, κ and κ_0 when considered as functions of the scaled coordinates $\lambda^{5/4}X$ and z. The results are, therefore, quite universal and, in particular, apply to any flow originating from a two-dimensional upstream boundary layer with $O(1)$ wall shear. Boundary layer profiles with near zero wall shear are not formally governed by the present asymptotic structure. The largest scaled roughness height, $3h/4 = 4$, considered in the following computations corresponds to an actual roughness height that lies between five and ten percent of the local boundary layer thickness. The unit Reynolds numbers R/x_0^* would lie between 10^5/meter and 10^6/meter for free stream speeds between 1.5 and 15 m/s in air and between 0.1 m/s and 1 m/s in water and, with a reference location of 0.1 m to 1.0 m, would require the use of plate lengths of about 2 meters in the relevant experiments, which is not too unreasonable. The roughness spacing would lie between 1.28 mm and 0.04 mm when R is

between 10^5 and 10^6 and $x_0^* = 0.1m$, and between 12.8 mm and 4 mm when R is between 10^5 and 10^6 and $x_0^* = 1.0m$.

Figure 4, which shows the wall shear distribution along the symmetry plane $z/l = \pi$ of the roughness element, gives some indication of the local flow field for $O(1)$ values of h. The shear perturbation downstream of the peak roughness height at *X* = 0 is somewhat similar to that shown in Fig. 2 of GSDC-2 for roughness element planforms with an O(1) aspect ratio. Both figures imply that there is a smooth retardation of the near wall flow behind the crest of the roughness element, followed by a local minimum in skin friction that leads to the slow recovery in near-wall velocities at large *X*. There are, however, several noteworthy differences between the wall shear distributions along the center plane in these two cases. First, there is a local (but not global) minimum in skin friction near $X \approx 1$ which corresponds to a rather weak perturbation relative to the unperturbed boundary layer (less than 5 percent change) while this downstream minimum was also the global skin friction minimum in GSDC-2 and the skin friction was nearly reduced to zero for the largest roughness height investigated in that study. Furthermore, the skin friction minimum in figure 2 of GSDC-2 was located much farther behind the roughness element crest than that shown in Fig. 4-indicating that the region of flow deceleration is considerably shorter in the present case. Finally, the wall shear approached the unperturbed wall shear monotonically for all roughness heights considered in GSDC-2, while Fig. 4 shows that, the wall shear perturbation actually crosses over into a positive region at a finite wake location when h > 3 (i.e., faster near wall flow than the unperturbed boundary layer) and eventually approaches a constant nonzero value at the larger values of *X* , which is consistent with the continuous growth in the streamwise velocity perturbation noted in subsection7.2 below.

These differences in the downstream wall shear are preceded by more dramatic differences in the upstream region. The upstream behavior was rather simple for the O(1) aspect ratio roughness elements considered in GSDC-2 and indicated that there was a slow, mild deceleration of the unperturbed boundary layer as it approached the roughness element followed by a relatively rapid acceleration up to just upstream of the roughness element crest. In contrast, the wall shear distribution in Fig. 4 suggests a more complex behavior involving a slow deceleration followed by an acceleration to a positive wall shear perturbation, which is, in turn, followed by another region of deceleration that leads to a global minimum in wall shear ahead of the roughness element, and eventually, a rapid acceleration up to the crest of the roughness element at *X* = 0. Another important difference between the two roughness shapes is related to the overall minimum in wall shear, which indicates a flow that is far from separation even at $\lambda^{1/3}h$ = 4 while the minimum skin friction for the same roughness height would have been less than 20 percent of the unperturbed wall shear (in comparison with the minimum of nearly two thirds of the unperturbed wall shear in Fig. 4) in the GSDC-2 case. The increased resistance to flow separation in the present case is consistent with the expected behavior for streamwise elongated roughness planforms, which provide a stronger spanwise relief for the flow approaching the surface obstacle. Given the robust, positive wall shear values for all roughness heights shown in Fig. 4, a spontaneous onset of unsteady vortex shedding within the wake region (as observed by Acarlar and Smith (1987) and Klebanoff et al. (1992) for roughness elements with O(1) aspect ratios) is deemed to be rather unlikely for the roughness shapes being considered in the present paper.

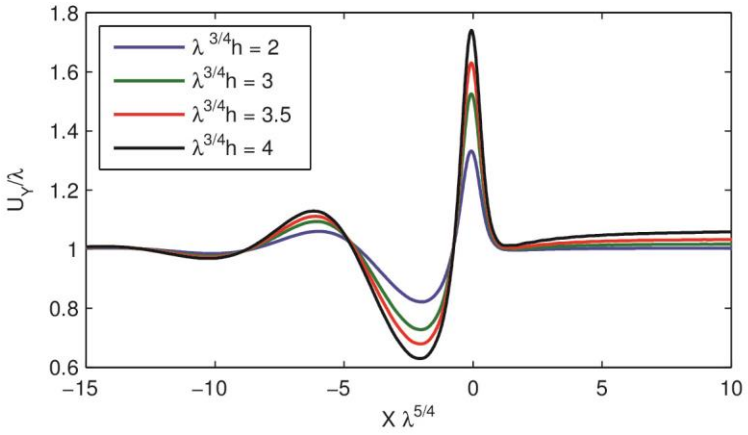

Figure 4) Scaled wall shear distribution along the symmetry plane $z = \pi l$ z of the roughness element for $d_0 = 1/2,\ d/\pi l = 1/2,\ \kappa = 2,\ d = 1$ and various values of h

Figure 5 displays the numerically computed spanwise variable component of the surface pressure normalized by λ^3. It is similar to figure 3 of GSDC-2, but carries the computations to slightly higher h values. The results show the increasing effects of nonlinearity as h becomes large, especially along the peaks and valleys of the streamwise pressure distribution. Although not shown here, the pressure perturbation decays monotonically upstream of the region plotted in figure 5, i.e., there is no correlation between the upstream pressure distribution and the local minimum and maximum in wall shear within the region $X\,\lambda^{5/4} < -5$ in figure 4. The acceleration of the near wall flow in between the local extrema is caused by a non-monotonic behavior in the spanwise pressure gradient that leads to lateral convergence of the perturbed flow within that region.

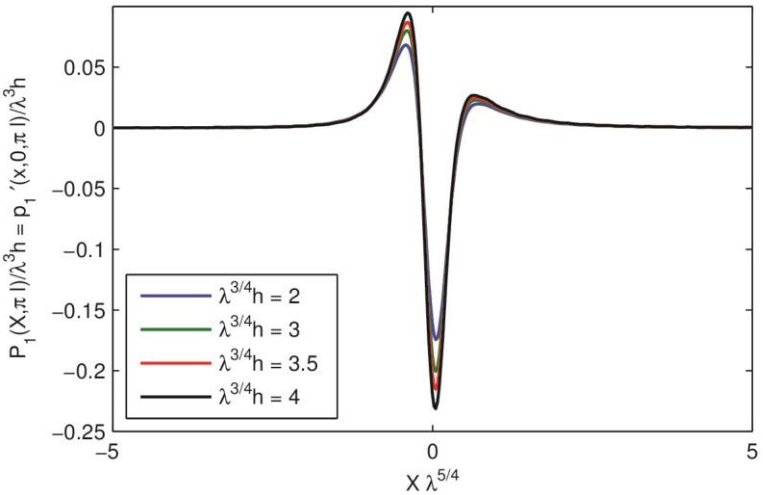

Figure 5 Normalized spanwise variable component of surface pressure distribution over the roughness elements computed from the nearfield solution for $d_0 = 1/2,\ d/\pi l = 1/2,\ \kappa = 2,$ $d = 1$ and various values of h

The scaled pressure perturbation p_1 is smaller than that for the roughness elements with O(1) aspect ratio planforms and the unscaled pressure perturbation is asymptotically smaller than the wall shear perturbation by a factor of ε^4 in the asymptotic regime of interest. Figure 4 shows that the unscaled normalized wall shear $\partial U / \partial Y$ varies between 0.055 and 0.134 when $R = 10^5$ and between 0.04 and 0.1 when $R = 10^6$,while Figure 5 shows that normalized unscaled wall pressure perturbation $\varepsilon^4 p_1 \ X, 0, \pi l$ varies between -2.71x10^{-4} and 1.085 x10^{-4} when $R = 10^5$ and between -8.6 x10^{-5} and 3.4 x10^{-5} when $R = 10^6$.

7.2 Intermediate scale flow

The intermediate scale flow (where X is large compared to the dimensions of the roughness elements but small compared to the downstream distance from the leading edge) is similar to that in GSDC-2, which shows that this flow is completely linear when the coefficient α in the asymptotic expansion is sufficiently large and that solutions only exist when $\alpha = n/3$, $\text{for } n = 1, 2, \ldots$. GSDC-1 obtained a linear solution for small h and found that $\alpha = 8/3$ and $\beta = 0$ while GSDc-2 extended the analysis to second order, i.e. to $O\left(h^2\right)$, and showed that $\alpha = 5/3$ and $\beta = 1$ in that case, which suggests that the small-h asymptotic expansion breaks down (or becomes disordered) when X becomes sufficiently large. Analogous behavior is expected to occur in the present case. In fact, an analysis similar to that given in GSDC-2 suggests that $p_1'\left(X, \mathrm{y}, z\right)$ should expand like

$$p_1'\left(X, \mathrm{y}, z\right) = \frac{h\hat{p}_1\left(y, z\right) + \ldots}{X^{8/3}} + \frac{h^2 \ln X^{1/3} \hat{p}_2\left(y, z\right) + \ldots}{X^{5/3}} + \ldots\ldots \qquad (7.6)$$

when $h \to 0$ and $X \to \infty$: which implies that

$$\lim_{X\to\infty} \lim_{h\to 0} p_1'\left(X, \mathrm{y}, z\right) \neq \lim_{h\to 0} \lim_{X\to\infty} p_1'\left(X, \mathrm{y}, z\right) \qquad (7.7)$$

The results given in GSDC-1 imply that the asymptotic wall layer flow can only become nonlinear when the spanwise variable component of the wall pressure decays like $1/X^{4/3}$. Section 5 shows that the resulting flow still possesses a similarity solution even though it is now (at least formally) governed by nonlinear equations. The asymptotic behavior of spanwise mean displacement $A\left(X\right)$ is primarily determined by the spanwise mean flow generated by the local nonlinear effects-which explains why the numbers are so small. Figure 6 clearly shows that it exhibits the assumed asymptotic behavior (5.1)with $\alpha_0 = 2/3$ and $\beta = 0$ as postulated in section 5 (in the paragraph below(5.13)).

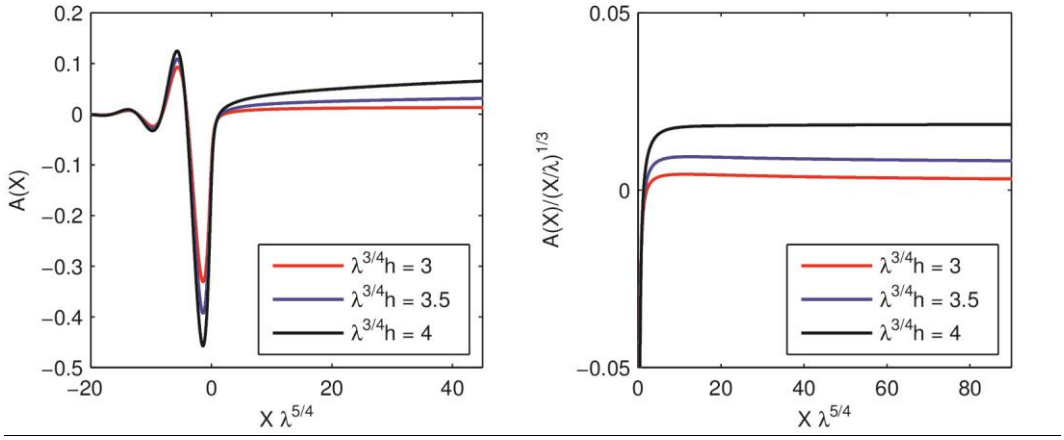

a) **b)**

Figure 6 a) $A(X)$ vs. X b) $A(X)/(X/\lambda)^{1/3}$ vs. X computed from the near field solution for $d_0 = 1/2,\ d/\pi l = 1/2,\ \kappa = 2,\ d = 1$ and h=3, 3.5 and 4

Figure 7, which is a plot of $p_1'(X,0,z)(X/\lambda)^{4/3}$ in the range $1000 < X\lambda^{5/4} < 3500$ and $p_1'(X,0,z)(X/\lambda)^{5/3}$ in the range $50 < X\lambda^{5/4} < 400$, with $z = \pi l$ shows that the spanwise variable wall pressure eventually decays like $X^{-4/3}$ when X becomes very large and that it exhibits the $X^{-5/3}$ decay found in GSDC-2 at moderately large values of X. This verifies that $p_1'(X,0,z)$ exhibits the limiting behavior identified in (5.41) with $\hat{p}_1(0,z) \gg \hat{p}(0,z)$.

It should be noted that only the spanwise variable component $p_1'(X,0,z)$ of the wall pressure contributes to the asymptotic wall layer flow, even though the corresponding spanwise mean component $P(X)$ of the pressure decays more slowly than the former. The intermediate scale wall layer flow, therefore becomes relatively generic at very large values of X and only depends on the near field flow in the vicinity of the roughness through the coefficient $\hat{p}(0,z)$ of the first term in the asymptotic expansion (5.41) of the spanwise variable component of the surface pressure $P_1(X,z) = p_1'(X,0,z)$.

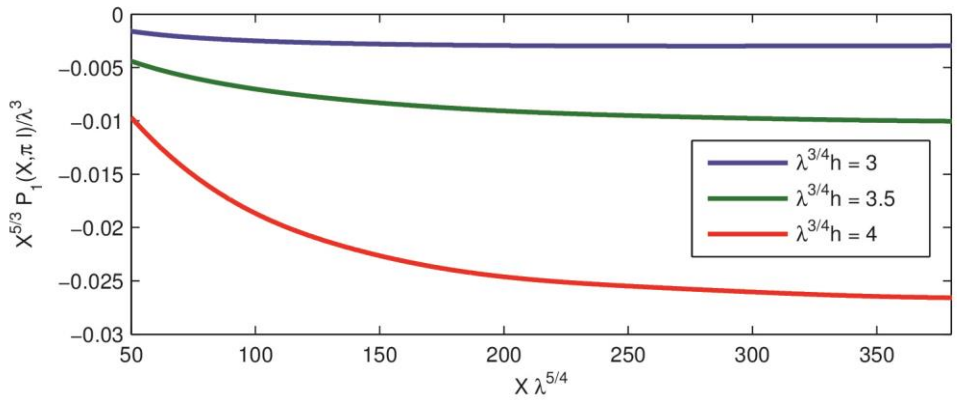

a)

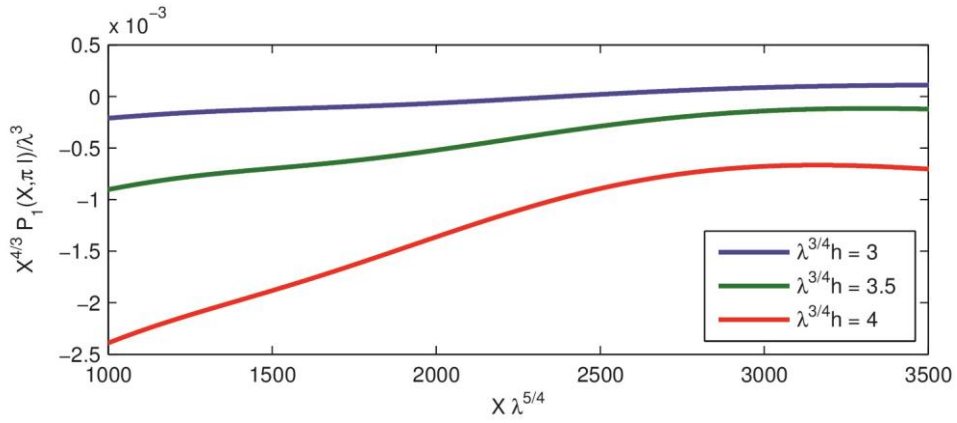

b)

Figure 7 Scaled surface pressure $p_1'(X,0,z)/\lambda^3 = P_1(X,z)/\lambda^3$ vs. $X\lambda^{5/4}$ computed from the near field solution directly behind the roughness element for $\lambda^{3/4}h$ =3, 3.5 and 4 and $d_0 = 1/2,\ d/\pi l = 1/2,\ \kappa$=2, d=1 a) $P_1(X,z)X^{5/3}/\lambda^3$ in the range $50 < X\lambda^{5/4} < 400$, b) $P_1(X,z)X^{4/3}/\lambda^3$ in the range $1000 < X\lambda^{5/4} < 3500$

The computations shown in this sub-section were very challenging numerically and required great care because i) the asymptotic (far downstream) growth of the dependent variables corresponds to a singular behavior of their Fourier transforms as $k \to 0$ and ii) because, as shown in figure 7, the final downstream asymptotic state is only achieved at very large downstream distances (even when h is fairly large) while the magnitude of the leading-order coefficient $\hat{p}(y,z)$ of the asymptotic pressure expansion (5.41) turns out to be exceedingly small relative to the coefficient $\hat{p}_1(y,z)$ of the second-order term.

The iterative solution constructed in Appendix A shows that the similarity solution will exist even when the coefficient $\hat{p}(0,z)$ of $1/X^{4/3}$ in the asymptotic expansion of spanwise variable component of the surface pressure becomes arbitrarily small and the intermediate scale flow becomes linear. This suggests that the spanwise variable pressure will exhibit this 4/3 decay rate even when $h \to 0$, which again implies that the inequality (7.7) should hold. This leads to the rather surprising conclusion that the true asymptotic behavior of the wall layer solution can only be found by considering the full nonlinear near-field solution no matter how small the roughness height h may be. This is, of course, distinctly different from the near field roughness scale nonlinearity considered in GSDC-2.

There are, therefore, two types of linearization that can be used to simplify the asymptotic solution of the nonlinear wall layer equations (4.5)-(4.7). The first is a linearization of the near field solution obtained by expanding in powers of h and the second is a linearization of the intermediate scale solution with $h = O(1)$. Unfortunately there does not appear to be any natural expansion parameter and therefore no formal asymptotic limit associated with this latter linearization. However, we capitalize on this linearization in Appendix A to construct a rapidly convergent iterative solution to the fully nonlinear equations(5.34), (5.36) and(5.39).

Figure 8 is a plot of the lowest order scaled asymptotic surface pressure coefficient $\hat{p}(0,z)$ in the asymptotic pressure expansion(5.41). It shows that the highest pressures directly behind the roughness element ($z=\pi l$) and, as expected, that it increases in magnitude with increasing h.

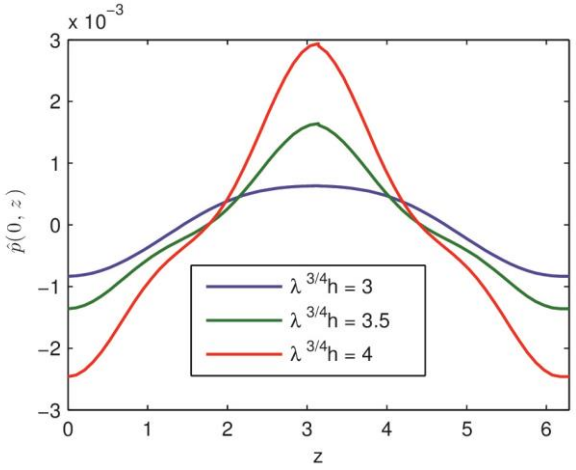

Figure 8 Scaled asymptotic surface pressure coefficient $\hat{p}(0,z)$ vs z computed from the nearfield solution for $d_0=1/2, d/\pi l=1/2, \kappa=2, d=1$ $\lambda^{3/4}h=3,3.5,4$

Equations (5.25) and (5.26) show that the ratio

$$\frac{U(X,Y,z)-\lambda Y}{\lambda Y}=\frac{\tilde{U}(\eta,z)-\eta}{\eta}, \tag{7.8}$$

of the maximum distortion velocity $U-\lambda Y$ to the local undisturbed velocity at $\eta=\eta_{\max}$ where

$$\tilde{U}(\eta_{\max},z)-\eta_{\max}=Max\left\{\left|\tilde{U}(\eta,z)-\eta\right| 0\le\eta<\infty;\ z=\text{constant}\right\} \tag{7.9}$$

does not actually grow in magnitude as $X\to\infty$ but merely moves up into a higher velocity region. In other words, the distortion velocity does not increase relative to the local mean flow velocity in the intermediate scale (overlap) region. It does, however increase like $X^{1/3}$ relative to the free stream velocity even though this only occurs because the $X^{1/3}$ increase in wall layer thickness causes distortion to move up into a higher undisturbed velocity region. So in this sense the distortion does not actually grow but merely persists over long streamwise distances until the action of viscosity in the BRE region causes it to decay on the long streamwise length scale. It does, however increase like $X^{1/3}$ relative to the free stream velocity. This is in contrast to the linear wake distortions considered in GSDC-1 and GSDC-2 which decay relative to the local mean flow.

Figure 9 is a plot of the streamwise distortion $\tilde{U}(\eta,z)-\eta$ vs η computed from the similarity solution at various values of z with $\hat{p}(0,z)$ calculated from the near field solution.

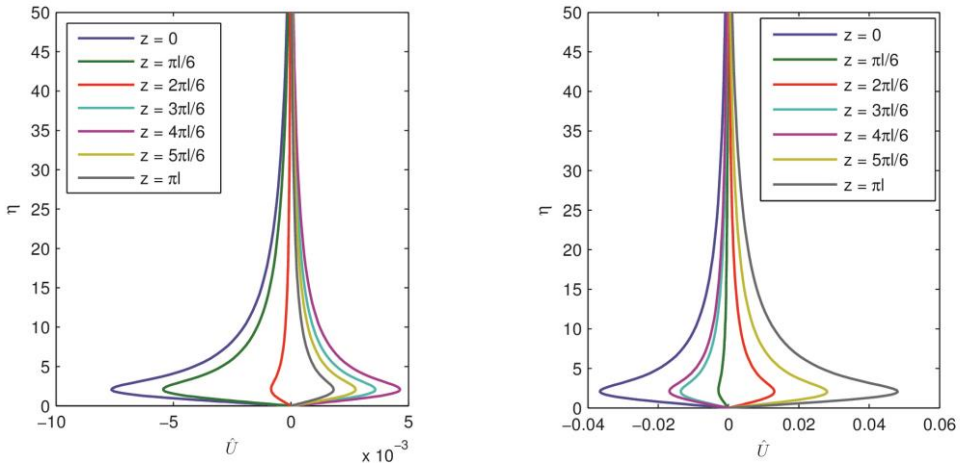

a) $\lambda^{3/4}h=3$ b) $\lambda^{3/4}h=4$

Figure 9 Streamwise distortion $\tilde{U}(\eta,z)-\eta$ vs η computed from the similarity solution with $\hat{p}(0,z)$ determined from the near field solution with $d_0=1/2,\ d/\pi l=1/2,\ \kappa=2,\ d=1$

The corresponding level surfaces of $\tilde{U}(\eta,z)-\eta$ are plotted against z in Figure 10.

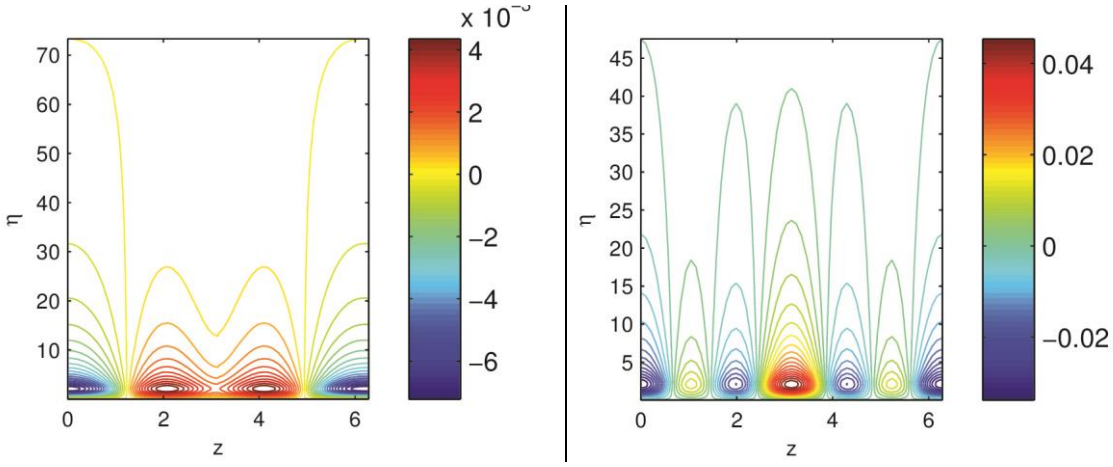

a) $\lambda^{3/4}h=3$ b) $\lambda^{3/4}h=4$

Figure 10 level surfaces of $\tilde{U}(\eta,z)-\eta$ as a function of z with $\hat{p}(0,z)$ determined from the nearfield solution with $d_0=1/2,\ d/\pi l=1/2,\ \kappa=2,\ d=1$

These figures show that the intermediate scale similarity solution(5.25) has a streak-like structure which is presumably due to a horseshoe vortex system at the leading edge. But the true nature of the downstream distortion can only be assessed by considering the flow in the longer outer region where the wall layer fills the entire boundary layer.

7.3 Far field solution

The flow in this region, where the normalized streamwise coordinate $x-1=O(1)$, is governed by the nonlinear BREs discussed in section 6. The relevant solution is obtained by using the

numerically computed wall pressure coefficients $\hat{p}(0,z)$ and $\hat{p}_1(0,z)$ in the intermediate scale expansion (5.41)to calculate the upstream boundary conditions for the boundary region equations that describe the flow on the long streamwise length scale $x-1$. The solutions are, therefore, less universal than the near field solutions discussed in the previous subsection, but the analysis can be extended to any flow originating from a two-dimensional upstream boundary layer by inserting the appropriate, externally determined streamwise pressure gradient term in the streamwise momentum equation(6.4).

Figure 11 is a plot of the second-order (linear) surface pressure coefficient $\hat{p}_1(0,z)$ determined from the best fit of the full two term expansion (5.41) to the numerically computed $p_1'(X,0,z)$. The figure shows that it increases fairly rapidly with increasing h. Comparison with figure 8 shows that $\hat{p}_1(0,z)$ is about an order of magnitude larger than the nonlinear coefficient $\hat{p}(0,z)$ even for the relatively large roughness heights considered in this paper --which means that, as noted at the end of section 6, the second term in the outer BRE expansion (6.2), which satisfies linearized equations, will be larger than the first when x is close to 1 and the Reynolds number is not too large. But, as shown below, the second term either remains constant or decays while the nonlinear term initially exhibits spatial growth and therefore becomes dominant over the long outer length scale on which the transient growth occurs. The figure also shows that the pressure maximum is no longer directly behind the roughness elements.

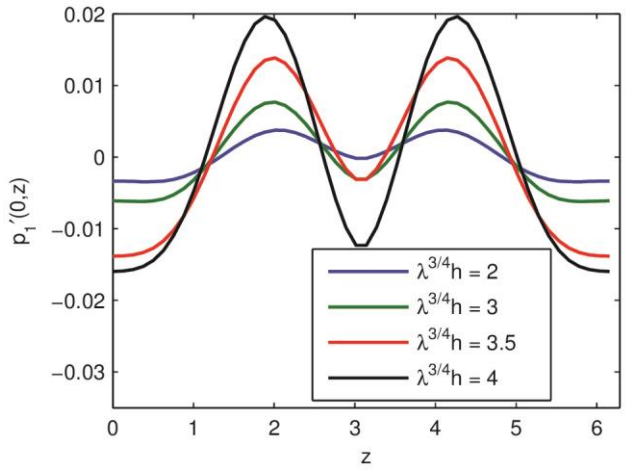

Figure 11 Plot of $\hat{p}_1(0,z)$ vs. z determined from the best fit of the full two term expansion (5.41) to the numerically computed $p_1'(X,0,z)$ for $d_0=1/2,\ d/\pi l=1/2,\ \kappa=2,\ d=1$ an d h=2, 3, 3.5 and 4

The nonlinear scale factor $\hat{p}(0,z)$ in (5.41) could be larger for other roughness shapes. But since it is quite small in the present case the nonlinear effects can be neglected when calculating the second-order solution to both the BRE solutions and the asymptotic near field (intermediate scale) flow. This means that the results can be well approximated by linearizing about the Blasius flow. The appropriate linearized BRE for the resulting linear $O(\varepsilon)$ term in the outer expansion (6.2) are given by equations (5.3)-(5.7) of GSDC-1 and the corresponding upstream

matching conditions, which are only given implicitly in that reference, are written out explicitly in Appendix B for convenience.

The extension of the GSDC-1and GSDC-2 equi-planform-dimension solution to the fully nonlinear case, which was precluded in those references by the requirement that the near field pressure vanish at downstream infinity, is discussed in Appendix C. The results show, among other things, that the solution to this problem would also lead to an asymptotic pressure perturbation of the form (5.41) in the large X limit.

The present results show that the leading order terms in (5.41) and (5.42) are quite small (at least for h and R-values being considered here) and $\hat{p}(0,z)$ can be set to zero when calculating the second order term in these expansions—which is precisely what was done in GSDC-1 and GSDC-2. The present analysis, therefore, justifies the results given in GSDC-1.

Some typical streamwise velocity profiles computed from the BRE equations with the upstream boundary conditions determined by the numerically computed pressure coefficients shown in figures 8 and 11 are displayed in Figures 12-20. Figure 12 is a plot of the streamwise velocity perturbation profiles produced by the first (nonlinear) term in the outer expansion (6.2) at the roughness centerline $z = \pi l$, and Figure 13 is a plot of the corresponding perturbation profiles between the adjacent roughness elements (at z = 0).

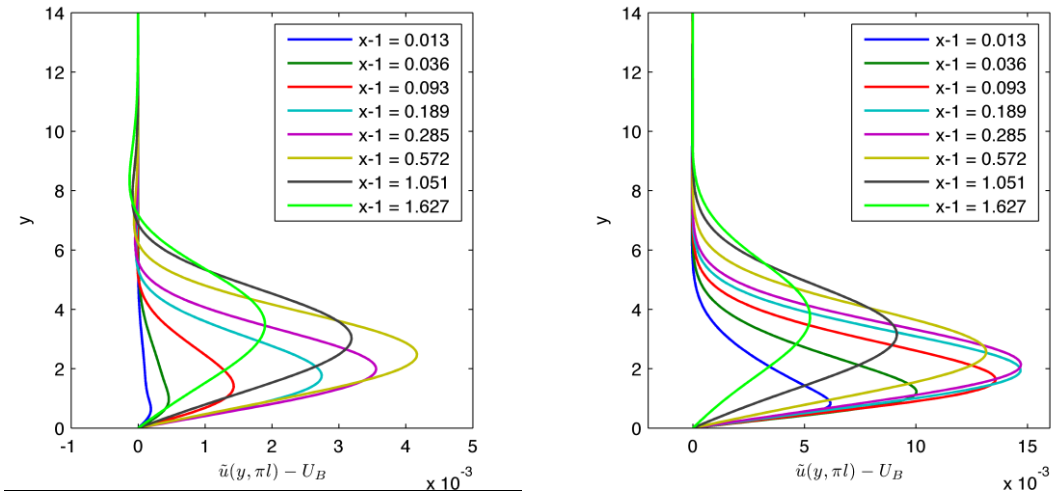

Part a) $\lambda^{3/4}h$ =3. Part b) $\lambda^{3/4}h$ =4

Figure 12. Scaled streamwise velocity distortion directly behind the roughness elements computed from the first term in the expansion (6.2) **for** $d_0 = 1/2,\ d/\pi l = 1/2,\ \kappa = 2,\ d = 1$

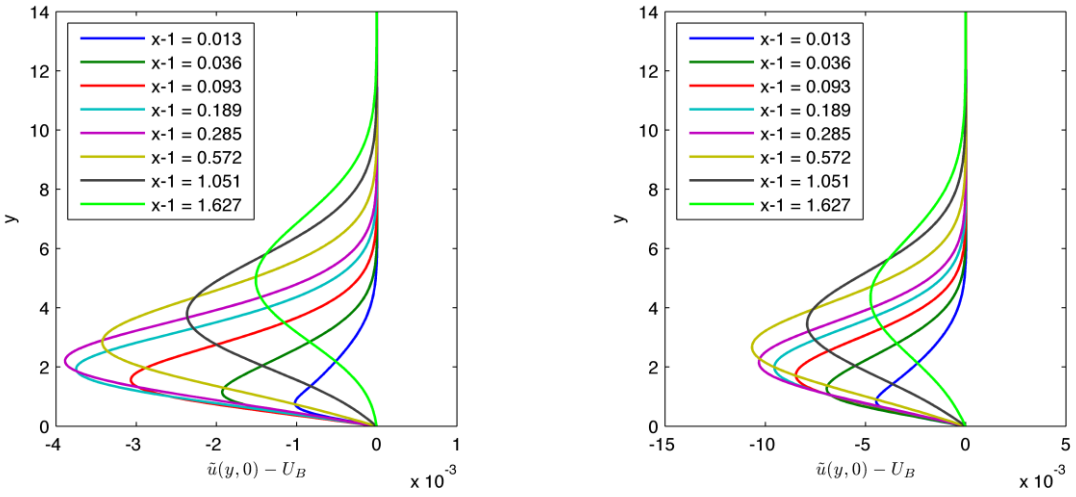

Part a) $\lambda^{3/4}h$ =3

Part b) $\lambda^{3/4}h$ =4

Figure 13. Same as Figure 12, except $z = 0$ instead of $z = \pi l$.

Figures 12 and 13 clearly show that the non-linear (i.e. lowest order) term in the outer expansion (6.2) continues to grow over a significant distance before it begins to decay. The peak velocity perturbation is found at x-1 = 0.285 or x-1 = 0.572 for both $\lambda^{3/4}h$ = 3 and $\lambda^{3/4}h$ = 4, depending on the spanwise location and roughness height parameter. In other words, it exhibits transient growth over the long streamwise length scale $x-1$. They also show that the corresponding velocity profiles are jet-like directly behind the roughness elements and wake-like between the elements. Previous studies have shown that that the velocity profiles behind the roughness elements can be either jet-like or wake-lake depending on nature of the horseshoe vortex system (formed by the wrapping of spanwise vorticity lines in the incoming boundary layer) which, in turn, depends on the shape parameters of the roughness elements. (See Fransson et al., 2004 and Choudhari & Fischer, 2005 for a summary of the available literature.) The jet-like profiles occur because the horse shoe vortex system induces a down welling along the roughness centerline, which accelerates the flow directly behind the roughness elements and progressively counteracts the velocity defect created by the upstream flow retardation due to the presence of the surface obstacle. The figures also show that the velocity minimum/maximum moves up towards the outer edge of the boundary layer with increasing downstream distance. The peak velocity perturbation more than doubles in magnitude with an approximately 33 percent increase in roughness height from $\lambda^{3/4}h$ = 3 to $\lambda^{3/4}h$ = 4, indicating the strongly nonlinear dependence of wake perturbations on the roughness height parameter. Similar dependence has been previously found for roughness element planforms with an O(1) aspect ratio (White and Ergin 2003).

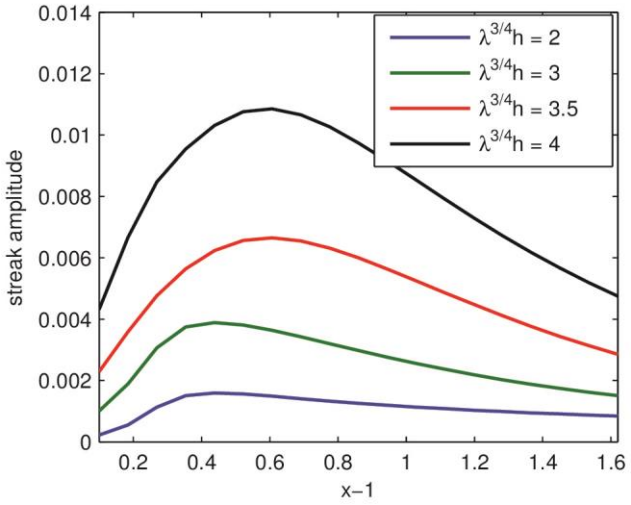

Figure 14 Peak velocity distribution directly behind roughness element computed from the first term in the expansion (6.2) for $d_0 = 1/2,\ d/\pi l = 1/2,\ \kappa = 2,\ d = 1$

The transient growth behavior on the longer BRE scale is more clearly depicted in figure14, wherein a representative streak amplitude is plotted as a function of $x-1$ for selected values of the roughness height parameter $h\lambda^{3/4}$. For simplicity, this amplitude is defined as the peak streamwise velocity perturbation directly behind the roughness element, which is not identical to the amplitude measure used by Fransson et al. (2004), but is expected to closely approximate the latter metric over most of the wake region of interest. Figure 14 shows that the maximum streak amplitude is achieved at downstream distances from the roughness elements that are comparable to their distance from the leading edge. The figure also shows that the distance from the roughness array to the peak amplitude location (i.e., the approximate range of locations over which transient growth occurs) increases with roughness height. These findings are in qualitative agreement with the experimental measurements by Fransson et al. (2004) and Fransson and Talamelli (2012) for roughness elements in the form of cylindrical disks and micro vortex generators, respectively.

Figure 15 is a plot of the streamwise velocity perturbation profiles computed from the second term in the expansion outer expansion (6.2) at the roughness centerline $z = \pi l$, and Figure 16 is a plot of the corresponding perturbation profiles between the adjacent roughness elements (at z =0).

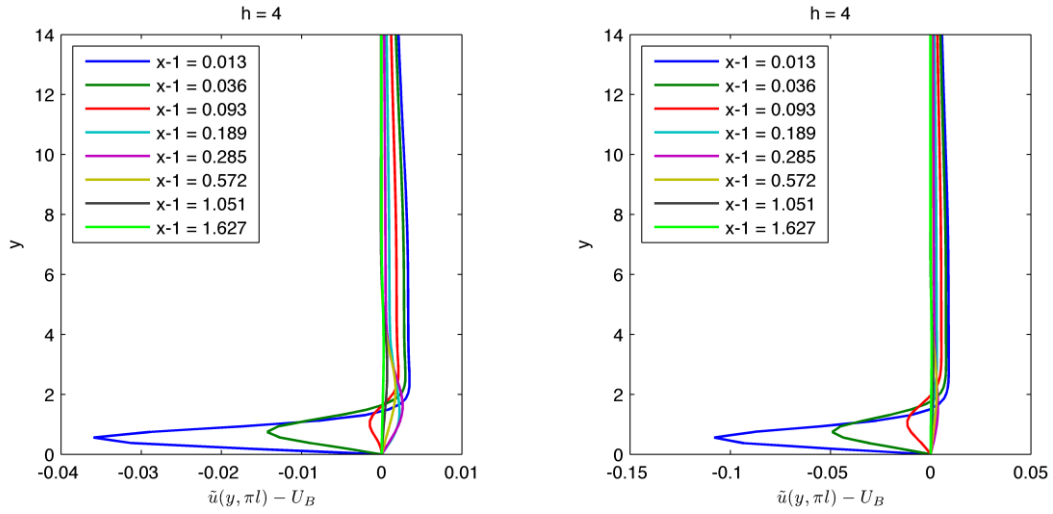

Part a) $\lambda^{3/4}h$ =3. Part b) $\lambda^{3/4}h$ =4

Figure 15. Scaled streamwise velocity distortion directly behind the roughness elements computed from the second (linear) term in the expansion (6.2) for $d_0 = 1/2,\ d/\pi l = 1/2,\ \kappa = 2,\ d = 1$

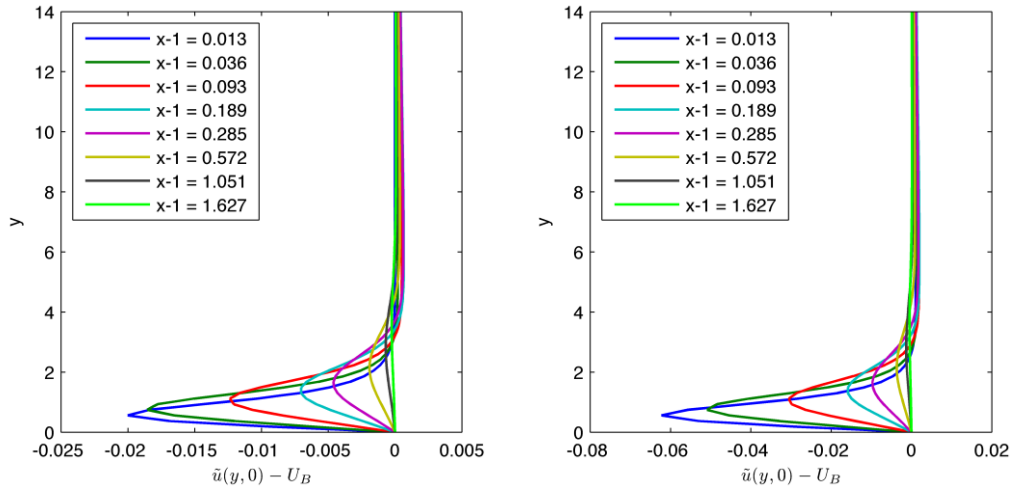

Part a) $\lambda^{3/4}h$ =3 Part b) $\lambda^{3/4}h$ =4

Figure 16. Same as Figure 15, except $z = 0$ instead of $z = \pi l$.

These figures show that while the linear (second) term in the outer expansion (6.2) is much larger than the non-linear term, the velocity perturbation either remains constant or decays with increasing downstream distance-which means that *the nonlinear term will eventually dominate over the linear contribution*. They also show that while the velocity profiles between the roughness elements are always wake-like the profiles directly behind the elements change from wake-like to jet-like with increasing downstream distance.

This behavior is shown more clearly in figures 17 and 18, with figure 16 showing the streamwise velocity perturbation computed from the full two term expansion(6.2) at the roughness centerline $z = \pi l$ and figure 18 showing corresponding perturbation profiles at a spanwise

location in between the adjacent roughness elements (at z = 0). The maximum streak amplitudes are rather small compared to the free stream velocity, but the present results suggest that other roughness shapes and larger height parameters can lead to much stronger streaks without producing any flow separation in the vicinity of the roughness element.

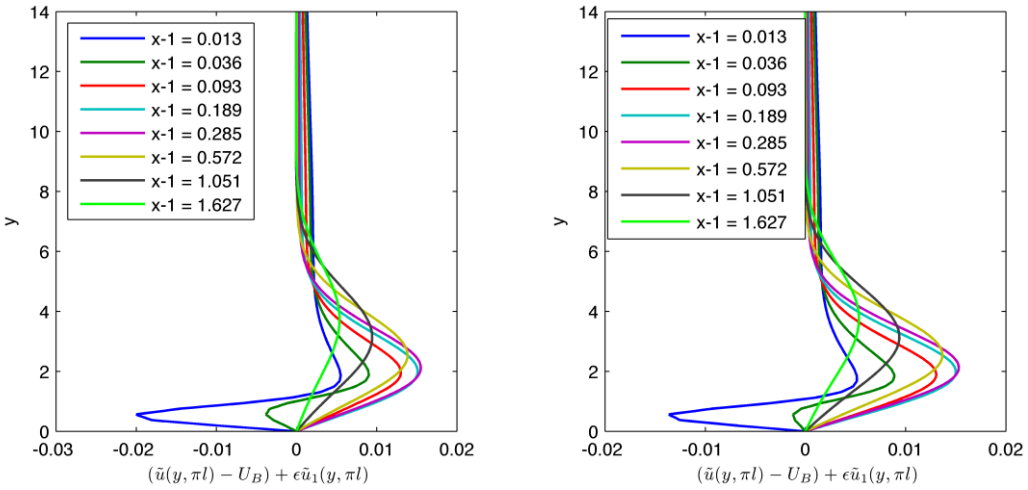

Part a) $R = 10^5$ Part b) $R = 10^6$

Figure 17. Scaled streamwise velocity distortion directly behind the roughness elements computed from the two term expansion (6.2) for $\lambda^{3/4}h$ =4, $d_0 = 1/2,\ d/\pi l = 1/2,\ \kappa = 2,\ d = 1$ a) $R = 10^5$ and b) $R = 10^6$

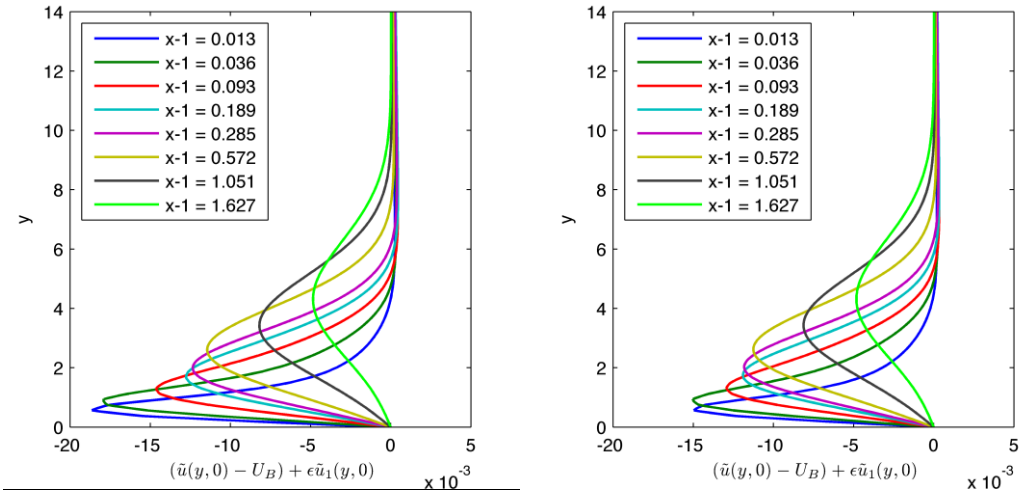

Part a) $R = 10^5$ Part b) $R = 10^6$

Figure 18. Same as Figure 16, except $z = 0$ instead of $z = \pi l$.

Figures 19 and 20 show contours of constant streamwise velocity perturbation over the cross section of the wake at various values of x, with the Reynolds number R equal to 10^5 in the first of these and 10^6 in the second. Visual inspection of these figures suggests that the initial wake structure is dominated by the second harmonic in z, which coincides with the spanwise width of the roughness element. However, the fundamental mode corresponding to the spanwise

spacing between the adjacent roughness elements becomes dominant farther downstream which is consistent with the numerical simulations of Choudhari and Fischer (2005). (A strong second harmonic would produce additional peaks and valleys within the contours.). This implies that the emergence of the fundamental mode as the dominant harmonic takes place over the longer scale of the BRE region since Figure 10 shows the asymptotic nearfield solution is dominated by the second harmonic.

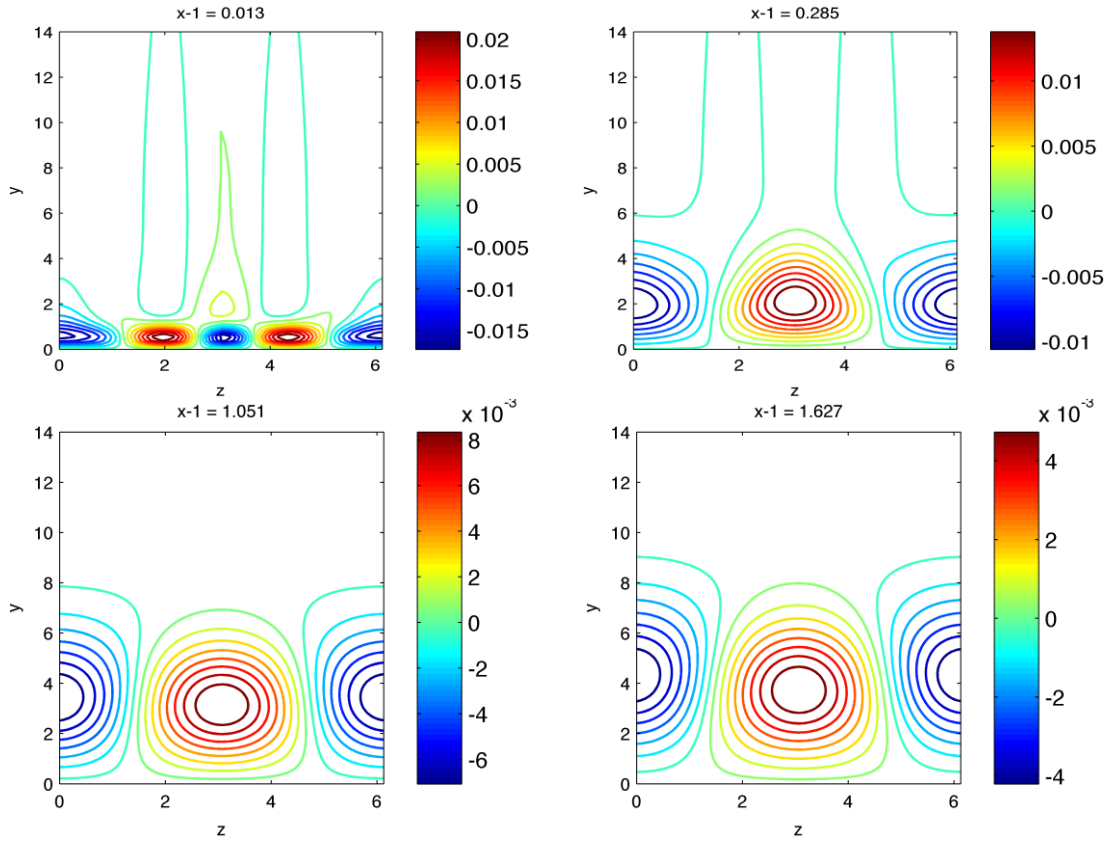

Figure 19. Contour plot of surfaces of constant streamwise velocity perturbation at various values of x, with $\lambda^{3/4}h = 4$, $d_0 = 1/2$, $d/\pi l = 1/2$, $\kappa = 2$, $d = 1$ and $R = 10^5$

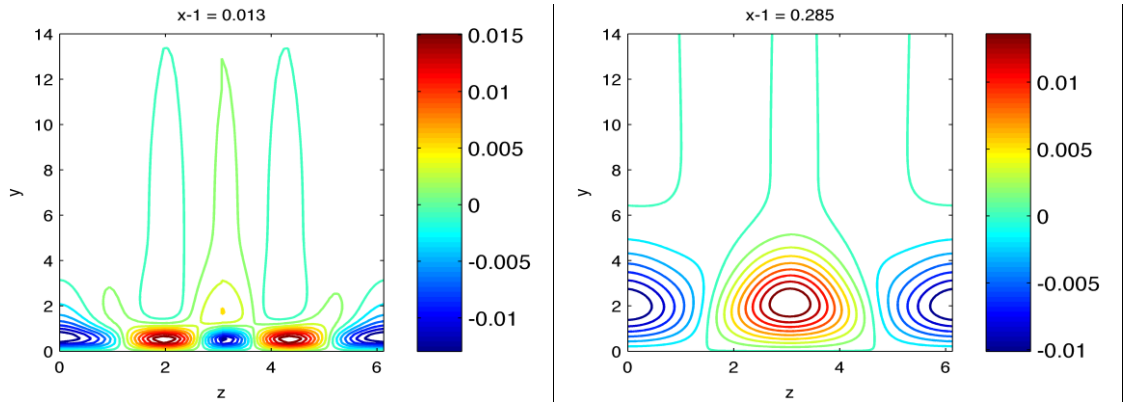

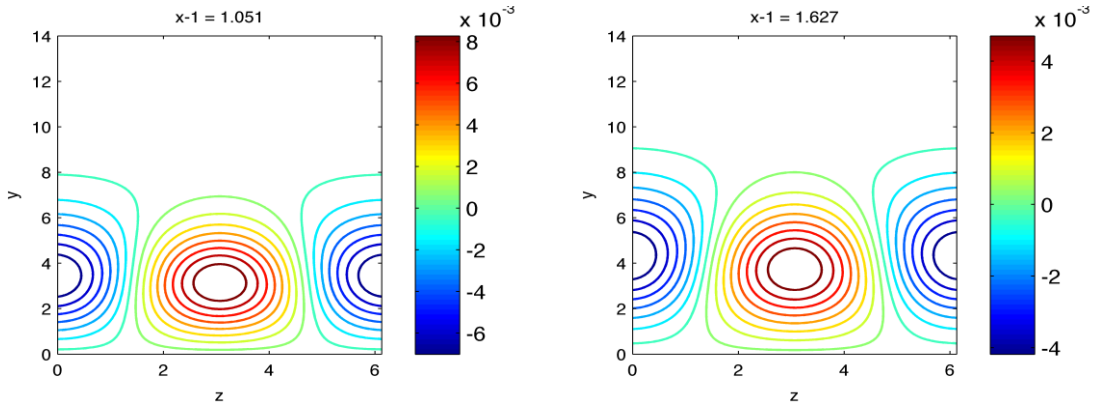

Figure 20. Same as figure 19, except for $R=10^6$

The wake evolution in figures 18 and 19 further shows that the peak in the streamwise velocity distortion is initially concentrated in the wall layer in the intermediate (algebraic growth) region, $X \gg 1, \quad x-1 \ll 1$ but again moves out into the main boundary layer at downstream locations and that the lowest order (nonlinear) contribution eventually dominates and causes the total velocity perturbation to exhibit streamwise growth. But even the total streamwise velocity perturbation eventually saturates and undergoes a slow decay with further increase downstream distance —which is why we refer to this outer region as the transient growth region.

8. Summary and Concluding Remarks

This paper is based on a high Reynolds number asymptotic solution for the flow over a spanwise periodic array of relatively small roughness elements. The roughness elements are assumed to be elongated in the streamwise direction with both the spanwise dimension and the array spacing being of the order of the local boundary-layer thickness and the streamwise dimension being of the order of the local triple deck length scale. The roughness height is assumed to be small enough to produce only local separation. The problem is formulated for a flat plate boundary layer but the results can easily be extended to boundary layers with arbitrary pressure gradient by inserting an appropriate streamwise pressure gradient term in the BRE (6.4) which only depends on the slow streamwise coordinate x and can be computed from the external potential flow. The results show that the downstream wakes are comprised of positive and negative streak-like perturbations that exhibit algebraic growth and that their maximum amplitude increases with Reynolds number.

The maximum streak amplitudes are somewhat small (less than two percent of the free stream velocity) at finite values of the Reynolds number. However, suitable modifications to the roughness shape should increase the streak amplitudes. And more importantly, the above streak amplitudes can be achieved in the present asymptotic regime without any flow reversal that could otherwise precipitate an onset of other unsteady phenomena via Kelvin Helmholtz instabilities of the separated flow. This finding makes the present regime particularly relevant to potential control of Tollmien-Schlichting waves via the stationary streaks. It is, however, worth noting that Goldstein & Wundrow (1965) and Wu & Luo ((2003) both showed that even small amplitude streaks can support inviscid instabilities.

Transient growth over long streamwise length scales of the order of the downstream distance from the leading edge was identified by Andersson et al. (1999), Luchini (2000), and Tumin and Reshotko (2001) in the context of the linearized boundary region equations. But these studies

were based on optimal growth theory which addresses a hypothetical initial value problem that determines the initial disturbance profiles at a given station that would maximize the energy growth up to a specified downstream location. It does not involve any consideration of whether or not the optimal initial disturbance profiles will be excited in practice as a result of naturally occurring external disturbances. In fact, it does not even provide any information about what type of actuation could be used to excite a disturbance field that would match the optimal growth predictions starting from the initial station of interest. The present paper treats a concrete physical problem that can be easily simulated in an experiment. The resulting transient growth is, therefore, realizable. The present paper examines realizable transient growth behavior in the context of the nonlinear Boundary Region Equations together with a modified form of the usual interactive boundary layer equations and shows that the leading order streak-like velocity perturbations can exhibit a weaker, i.e., suboptimal growth of the form $X^{1/3}$ as $X \to \infty$ on the roughness scale before exhibiting transient growth on the longer downstream length scale. However, the second order term in the large-X asymptotic expansion, which does not exhibit streamwise growth, turns out to be numerically much larger than this term (at finite values of R) and, therefore, tends to dominate the intermediate scale flow as well as the initial behavior of the BRE solution in the downstream region. But, the initially small nonlinear term corresponding to the zeroth order BRE solution undergoes transient growth and eventually becomes dominant. So the algebraically growing solution, which is initially hidden in the background in the intermediate scale (algebraic growth) region eventually becomes dominant and produces transient growth on the outer BRE scale. While it would have been difficult to discover these results with a strictly numerical approach, the overall behavior of the present asymptotic solution is roughly consistent with the finite Reynolds number computations of Choudhari and Fischer (2005).

Since the theoretical formulation is valid for arbitrary roughness configurations, the present computations can easily be extended to other roughness shapes and, in particular, to compact shapes such as mini-vortex generators or circular disks, which are likely to result in flow separation at smaller values of roughness height than for the smoother shapes considered herein.

Appendix A Iterative solution to nonlinear problem

A.1 Basic equations

The comments following equation (5.40) suggest that $\tilde{W}$ will be a relatively small perturbation of the undisturbed flow $\tilde{U} = \eta$. We can capitalize on this by noting that the system(5.34),(5.36) and(5.39) shows that

$$\hat{U} \equiv \tilde{U} - \eta, \quad \hat{v} \equiv \tilde{v} + \frac{1}{3}\eta^2 = \tilde{V} - \frac{\eta}{3}\left(\tilde{U} - \eta\right) \tag{A.1}$$

are determined by

$$\frac{2}{3}\hat{U} + \hat{v}_\eta + \tilde{W}_z = 0, \tag{A.2}$$

$$\frac{1}{3}\left(\eta^2\tilde{W}\right)_\eta + \tilde{W}_{\eta\eta} = \left[e^{-\eta^3/9}\left(e^{\eta^3/9}W\right)_\eta\right]_\eta = \frac{\partial\hat{p}(0,z)}{\partial z} + \frac{\partial F}{\partial\eta} \tag{A.3}$$

$$-\frac{2}{3}\hat{U}\eta-\hat{\mathscr{v}}+\frac{1}{3}\eta^2\hat{U}_\eta+\hat{U}_{\eta\eta}=G \tag{A.4}$$

$$F\equiv\int_0^\eta\left[\left(\hat{\mathscr{v}}\tilde{W}\right)_\eta+\left(\tilde{W}^2\right)_z\right]d\eta=\hat{\mathscr{v}}^{(\eta)}\tilde{W}+\int_0^\eta\left(\tilde{W}^2\right)_z d\eta,\quad G\equiv\hat{U}^2+\left(\hat{\mathscr{v}}\hat{U}\right)_\eta+\left(\tilde{W}\hat{U}\right)_z \tag{A.5}$$

together with the transverse boundary conditions implied by (5.30)-(5.32).

Equation(A.3) can be formally integrated to obtain

$$\tilde{W}=e^{-\eta^3/9}\frac{\partial\hat{p}(0,z)}{\partial z}\int_0^\eta\eta e^{\eta^3/9}d\eta+e^{-\eta^3/9}\int_0^\eta e^{\tilde{\eta}^3/9}F(\tilde{\eta},z)d\tilde{\eta}$$
$$+\tilde{a}(z)e^{-\eta^3/9}\int_0^\eta e^{\eta^3/9}d\eta \tag{A.6}$$

which satisfies the boundary condition (5.31), since successive integrations by parts shows that

$$e^{-\eta^3/9}\int_0^\eta\eta e^{\eta^3/9}d\eta=\frac{3}{\eta}+\frac{9}{\eta^4}+\ldots..\to 0,\quad e^{-\eta^3/9}\int_0^\eta e^{\eta^3/9}d\eta=\frac{3}{\eta^2}+\frac{2\bullet 9}{\eta^5}+\ldots.\to 0 \tag{A.7}$$

as $\eta\to\infty$.

Eliminating $\hat{\mathscr{v}}$ on the left side of (A.4) shows that

$$e^{-\eta^3/9}\left(e^{\eta^3/9}\hat{U}_{\eta\eta}\right)_\eta+\tilde{W}_z=\frac{\partial G}{\partial\eta} \tag{A.8}$$

which upon integrating with respect to η, using(A.1),(5.29) and (5.30), and integrating the result by parts shows that

$$\hat{U}_{\eta\eta}=-\frac{\partial^2\hat{p}(0,z)}{\partial z^2}e^{-\eta^3/9}\int_0^\eta\bar{\eta}(\eta-\bar{\eta})e^{\bar{\eta}^3/9}d\bar{\eta}-e^{-\eta^3/9}\int_0^\eta(\eta-\bar{\eta})e^{\bar{\eta}^3/9}\frac{\partial F(z,\bar{\eta})}{\partial z}d\bar{\eta}$$

$$-\frac{d\tilde{a}(z)}{dz}e^{-\eta^3/9}\int_0^\eta(\eta-\tilde{\eta})e^{\tilde{\eta}^3/9}d\tilde{\eta}+e^{-\eta^3/9}\int_0^\eta e^{\tilde{\eta}^3/9}\frac{\partial\tilde{G}}{\partial\tilde{\eta}}d\tilde{\eta} \tag{A.9}$$

and it follows from(A.1), (5.30)and (5.32)that

$$\hat{U}=\frac{\partial^2\hat{p}(0,z)}{\partial z^2}\int_0^{\eta}\int_{\eta}^{\infty}\left[\int_0^{\tilde{\eta}}\tilde{\tilde{\eta}}\left(\tilde{\eta}-\tilde{\tilde{\eta}}\right)e^{\left(\tilde{\tilde{\eta}}^3-\tilde{\eta}^3\right)/9}d\tilde{\tilde{\eta}}\right]d\tilde{\eta}d\eta$$

$$+\int_0^{\eta}\int_{\eta}^{\infty}e^{-\bar{\bar{\eta}}^3/9}\left[\int_0^{\bar{\bar{\eta}}}\left(\bar{\bar{\eta}}-\bar{\eta}\right)e^{\bar{\eta}^3/9}\frac{\partial F\left(z,\bar{\eta}\right)}{\partial z}d\bar{\eta}\right]d\bar{\bar{\eta}}d\eta$$

$$+\frac{d\tilde{a}(z)}{dz}\int_0^{\eta}\int_{\eta}^{\infty}e^{-\bar{\bar{\eta}}^3/9}\int_0^{\bar{\bar{\eta}}}\left(\bar{\bar{\eta}}-\tilde{\eta}\right)e^{\tilde{\eta}^3/9}d\tilde{\eta}d\bar{\bar{\eta}}d\eta-\int_0^{\eta}\int_{\eta}^{\infty}e^{-\bar{\bar{\eta}}^3/9}\int_0^{\bar{\bar{\eta}}}e^{\tilde{\eta}^3/9}\frac{\partial G}{\partial\tilde{\eta}}d\tilde{\eta}d\bar{\eta}d\eta \qquad \text{(A.10)}$$

which will satisfy all the transverse boundary conditions provided $d\bar{a}(z)/dz$ and $\hat{A}$ satisfy the solvability condition

$$\frac{d\tilde{a}(z)}{dz}\int_0^{\infty}\eta\left[\int_0^{\eta}\left(\eta-\tilde{\tilde{\eta}}\right)e^{\left(\tilde{\tilde{\eta}}^3-\eta^3\right)/9}d\tilde{\tilde{\eta}}\right]d\eta=-\frac{\partial^2\hat{p}(0,z)}{\partial z^2}\int_0^{\infty}\eta\left[\int_0^{\eta}\tilde{\tilde{\eta}}\left(\eta-\tilde{\tilde{\eta}}\right)e^{\left(\tilde{\tilde{\eta}}^3-\eta^3\right)/9}d\tilde{\tilde{\eta}}\right]d\eta$$

$$-\int_0^{\infty}\eta\int_0^{\eta}e^{\left(\tilde{\eta}^3-\eta^3\right)/9}\left[\left(\eta-\tilde{\eta}\right)\frac{\partial F\ \left(z,\tilde{\eta}\right)}{\partial z}-\frac{\partial G\left(z,\tilde{\eta}\right)}{\partial\tilde{\eta}}\right]d\tilde{\eta}d\eta-\hat{A} \qquad \text{(A.11)}$$

where we have again integrated by parts to obtain this result.

A.2 numerical procedure

It now follows from(5.37)(A.2),(A.5)- (A.9) and (A.11)that the nonlinear problem can be solved iteratively by using the following equations to determine the determine the nth approximation $\tilde{a}^{(n)}(z),\tilde{W}^{(n)},\hat{U}^{(n)},\hat{V}^{(n)}$ to $a(z),\tilde{W},\hat{U},\hat{V}$

$$\frac{d\tilde{a}^{(n)}(z)}{dz}=\frac{\partial^2\hat{p}(0,z)}{\partial z^2}\Pi$$

$$-\frac{-\int_0^{\infty}\eta\int_0^{\eta}e^{\left(\tilde{\eta}^3-\eta^3\right)/9}\left[\left(\eta-\tilde{\eta}\right)\frac{\partial F^{(n-1)}\left(z,\tilde{\eta}\right)}{\partial z}-\frac{\partial G^{(n-1)}\left(z,\tilde{\eta}\right)}{\partial\tilde{\eta}}\right]d\tilde{\eta}d\eta-\hat{A}^{(n)}}{\int_0^{\infty}\eta\int_0^{\eta}e^{\left(\tilde{\eta}^3-\eta^3\right)/9}\left(\eta-\tilde{\eta}\right)d\tilde{\eta}d\eta} \qquad \text{(A.12)}$$

The preceding equations suggest the following iteration procedure be used to determine $\tilde{W}^{(n)}$ and $\tilde{U}^{(n)}$

$$\tilde{W}^{(n)}=e^{-\eta^3/9}\left\{\frac{\partial\hat{p}(0,z)}{\partial z}\int_0^{\eta}\eta e^{\eta^3/9}d\eta+\int_0^{\eta}e^{\eta^3/9}F^{(n-1)}(\eta)d\eta+\tilde{a}^{(n)}(z)\int_0^{\eta}e^{\eta^3/9}d\eta\right\} \qquad \text{(A.13)}$$

$$\hat{U}_{\eta\eta}^{(n)} = -e^{-\eta^3/9}\left\{\frac{\partial^2 \hat{p}(0,z)}{\partial z^2}\int_0^\eta \tilde{\eta}(\eta-\tilde{\eta})e^{\tilde{\eta}^3/9}d\tilde{\eta} + \frac{d\tilde{a}^{(n)}(z)}{dz}\int_0^\eta (\eta-\tilde{\eta})e^{\tilde{\eta}^3/9}d\tilde{\eta}\right.$$

$$\left. -\int_0^\eta e^{\tilde{\eta}^3/9}\left[\frac{\partial G^{(n-1)}(z,\tilde{\eta})}{\partial\tilde{\eta}} - (\eta-\tilde{\eta})\frac{\partial F^{(n-1)}(z,\tilde{\eta})}{\partial z}\right]d\tilde{\eta}\right\} \qquad \text{(A.14)}$$

$$\hat{U}^{(n)}(0,z) = 0, \quad \hat{U}_\eta^{(n)}(\eta,z) = \mathrm{O}\left(\eta^{-2}\right), \text{ as } \eta\to\infty \qquad \text{(A.15)}$$

$$\hat{\boldsymbol{v}}^{(n)} \equiv \tilde{V}^{(n)} - \frac{\eta}{3}\hat{U}^{(n)} = -\int_0^\eta\left(\frac{2}{3}\hat{U}^{(n)} + \tilde{W}_z^{(n)}\right)d\eta, \qquad \text{(A.16)}$$

for $n = 1,2,3....$, where

$$\Pi \equiv -\frac{\int_0^\infty \eta\left[\int_0^\eta \tilde{\eta}(\eta-\tilde{\eta})e^{\left(\tilde{\eta}^3-\eta^3\right)/9}d\tilde{\eta}\right]d\eta}{\int_0^\infty \eta\left[\int_0^\eta (\eta-\tilde{\eta})e^{\left(\tilde{\eta}^3-\eta^3\right)/9}d\tilde{\eta}\right]d\eta} \qquad \text{(A.17)}$$

$$F^{(0)}(z,\eta) = G^{(0)}(z,\eta) = A^{(1)} = 0 \qquad \text{(A.18)}$$

$$G^{(n)}(z,\eta) \equiv \frac{1}{3}\left[\hat{U}^{(n)}\right]^2 + \hat{\boldsymbol{v}}^{(n)}\hat{U}_\eta^{(n)} + \tilde{W}^{(n)}\hat{U}_z^{(n)} \qquad \text{(A.19)}$$

$$F^{(n)}(z,\eta) = \hat{\boldsymbol{v}}^{(n)}\tilde{W}^{(n)} + \frac{\partial}{\partial z}\int_0^\eta\left[\tilde{W}^{(n)}(z,\tilde{\eta})\right]^2 d\tilde{\eta} \qquad \text{(A.20)}$$

for $n = 1,2,3....$ .Note that that $\tilde{a}^{(n)}(z)$ is determined by the spanwise variable component of (A.12) and can therefore be taken to have zero spanwise mean, while $\hat{A}^{(n)}$ is determined by the spanwise mean component of that equation.

Appendix B Summary of upstream matching conditions for 2nd order BRE solution

$$\tilde{p}(x,y,z) \to \frac{\lambda^{5/3}\hat{p}(y,z)}{(x-1)^{5/3}} \qquad \text{(B.1)}$$

$$\tilde{u} \to (x-1)^{1/3}\tilde{u}_1(y,z) + \lambda\,\tilde{U}_1(\eta,z) + \frac{3^2\lambda^{2/3}}{2}\hat{p}_{1zz}(0,z)/y \qquad \text{(B.2)}$$

$$\tilde{v}(\mathrm{x},y,z)\to\frac{1}{(x-1)^{2/3}}\left\{\tilde{v}_1(y,z)-\frac{3\lambda^{2/3}}{2}\frac{\partial^2}{\partial z^2}\hat{p}_1(0,z)-\lambda^{2/3}\tilde{V}_1(\eta,z)\right\} \quad \text{(B.3)}$$

$$\tilde{w}(x,y,z)\to\frac{1}{(x-1)}\left\{(x-1)^{1/3}\left[\tilde{w}_1(y,z)-\frac{3\lambda^{2/3}}{2y}\frac{\partial\hat{p}(0,z)}{\partial z}\right]+\lambda\tilde{W}_1(\eta,z)\right\}, \quad \text{(B.4)}$$

$$\frac{2}{3}U_B(y)\tilde{u}_1+\tilde{v}_1U_B'(y)=0, \quad \text{(B.5)}$$

$$\frac{2}{3}U_B(y)\begin{Bmatrix}\tilde{v}_1\\ \tilde{w}_1\end{Bmatrix}=\lambda^{5/3}\begin{Bmatrix}\hat{p}_{1y}\\ \hat{p}_{1z}\end{Bmatrix}. \quad \text{(B.6)}$$

$$\tilde{U}_1(\eta,z)=\frac{\partial^2\hat{p}_1(0,z)}{\partial z^2}\frac{3}{2}\left[\int_0^\eta e^{-\tilde{\eta}^3/9}\int_0^{\tilde{\eta}}e^{\tilde{\tilde{\eta}}^3/9}d\tilde{\tilde{\eta}}d\tilde{\eta}\right.$$

$$\left.+\frac{\left[\Gamma(1/3)\right]^2\sqrt{3}}{2\pi3^{1/3}}\int_0^\eta e^{-\eta^3/9}U(1/3,2/3,\eta^3/9)d\eta-B_0\int_0^\eta e^{-\tilde{\eta}^3/9}d\tilde{\eta}\right\}\Bigg] \quad \text{(B.7)}$$

$$\tilde{V}_1=\frac{\partial^2\hat{p}_1(0,z)}{\partial z^2}\left[\frac{3}{2}-\frac{\left[\Gamma(1/3)\right]^2\sqrt{3}}{4\pi3^{4/3}}e^{-\eta^3/9}\eta^2U(4/3,5/3,\eta^3/9)\right] \quad \text{(B.8)}$$

$$\tilde{W}_1=-\frac{\partial\hat{p}_1(0,z)}{\partial z}\frac{\eta}{2}e^{-\eta^3/9}\left(\int_0^\eta e^{\tilde{\eta}^3/9}d\tilde{\eta}-B_0\right) \quad \text{(B.9)}$$

where

$$B_0\equiv\frac{\displaystyle\int_0^\infty\left(e^{-\tilde{\eta}^3/9}\int_0^{\tilde{\eta}}e^{\tilde{\tilde{\eta}}^3/9}d\tilde{\tilde{\eta}}\right)d\tilde{\eta}+\frac{\left[\Gamma(1/3)\right]^2\sqrt{3}}{2\pi3^{1/3}}\int_0^\infty e^{-\eta^3/9}U(1/3,2/3,\eta^3/9)d\eta}{\displaystyle\int_0^\infty e^{-\tilde{\eta}^3/9}d\tilde{\eta}}\Bigg], \quad \text{(B.10)}$$

and $U(a,b,z)$ denotes the Hypergeometric function defined by (13.1.3) of Abramowitz & Stegun (1965).

C. Short roughness elements with similar streamwise and spanwise length scales

Instead of solving the near field boundary value problem described in sections3 and 4, we could consider the initial value problem obtained by setting roughness shape function $F(X,z)=0$ and specifying an upstream boundary condition at $X=0$. Since equations (5.14)-(5.21) are an exact solution to the main deck equations (3.10)-**Error! Reference source not found.** they can also be thought of as the leading terms in an $X\to 0$ asymptotic expansion of a solution to these equations and, therefore, be taken as the initial conditions for the complete boundary value problem which satisfies(2.5) at downstream infinity. But it is more interesting to consider the slightly different case where

$$P(X)\to\lambda^2\hat{P}(X/\lambda)^{2/3},\ X\to 0 \qquad \text{(C.1)}$$

which corresponds to setting $\alpha_0=-2/3$ in(5.1) rather than to +2/3 as was done previously. It then follows from(5.1), (5.10)and (5.13) (which remain valid when the $\sim$ symbol is replaced by an equals sign) that

$$A(X)\to A_0+\hat{A}(X/\lambda)^{5/3},\ \text{as } X\to 0 \qquad \text{(C.2)}$$

where, as before, $\hat{A}$ is a constant related to $\hat{P}$. The solution is still exact but the spanwise mean conditions (5.14)and (5.15) must be replaced by

$$u_0=U_B'(y)\left[A_0+\hat{A}(X/\lambda)^{5/3}\right], \qquad \text{(C.3)}$$

$$v_0=-5U_B(y)\hat{A}(X/\lambda)^{2/3}/\lambda 3, \qquad \text{(C.4)}$$

The wall layer flow still possess the exact similarity solution (5.25)but with the streamwise momentum equation(5.29) replaced by

$$\frac{1}{3}\tilde{U}\left(\tilde{U}-\eta\tilde{U}_\eta\right)+\tilde{V}\tilde{U}_\eta+\tilde{W}\tilde{U}_z=-\frac{1}{3}\hat{p}_0+\tilde{U}_{\eta\eta}, \qquad \text{(C.5)}$$

Introducing the inner variable

$$X=\bar{X}(\bar{\varepsilon}/\varepsilon)^3, \qquad \text{(C.6)}$$

where $\bar{\varepsilon}\equiv R^{-1/6}$, into(5.18)-(5.21),(5.25)and (C.1)-(C.4) shows the result will match onto the two layer inner expansion

$$\{u,v,w,p\}=\left\{U_B+\varepsilon\bar{U}_1(y),\bar{\varepsilon}^3V_B,0,0\right\}+\bar{\varepsilon}^2\left\{\bar{u}_0(\bar{X},y,z),\bar{v}_0(\bar{X},y,z)\right.$$
$$\left.,\bar{w}_0(\bar{X},y,z),\bar{p}_0(\bar{X},y,z)\right\}+\ldots\ldots, \qquad \text{(C.7)}$$

for $y=O(1)$ and

$$\{u,v,w,p\}=\bar{\varepsilon}\left\{\bar{U}(\bar{X},\bar{Y},z),\bar{\varepsilon}\bar{V}(\bar{X},\bar{Y},z),\bar{W}(\bar{X},\bar{Y},z),\bar{\varepsilon}\bar{P}(\bar{X},z)\right\}+\ldots.\,, \qquad \text{(C.8)}$$

for $\bar{Y} \equiv y/\bar{\varepsilon} = O(1)$, whose first order terms behave like

$$\bar{u}_0 \to U_B'(y)\hat{A}\left(\bar{X}/\lambda\right)^{5/3} - \frac{(3\lambda)^2\left(\bar{X}/\lambda\right)^{2/3}}{2}\frac{U_B'(y)}{U_B^2(y)}\frac{\partial}{\partial y}\hat{p}(y,z),$$

$$\bar{v}_0 \to -5U_B(y)\hat{A}\left(\bar{X}/\lambda\right)^{2/3}/3\lambda + \frac{3\lambda}{\left(\bar{X}/\lambda\right)^{1/3}U_B(y)}\frac{\partial\hat{p}(y,z)}{\partial y}, \qquad \text{(C.9)}$$

$$\bar{p}_0\left(\bar{X},y,z\right) \to \lambda^2\hat{p}_0\left(\bar{X}/\lambda\right)^{2/3} + \hat{p}(y,z)/\left(\bar{X}/\lambda\right)^{4/3}, \qquad \text{(C.10)}$$

$$\bar{w}_0\left(\bar{X},y,z\right) \to \frac{3\lambda}{\left(\bar{X}/\lambda\right)^{1/3}U_B(y)}\frac{\partial\hat{p}(y,z)}{\partial z}, \qquad \text{(C.11)}$$

as $\bar{X} \to \infty$ for $y = O(1)$ and like

$$\bar{W} \to \left(\bar{X}/\lambda\right)^{-2/3}\tilde{W}(\eta,z),\ \bar{U} \to \lambda\left(\bar{X}/\lambda\right)^{1/3}\tilde{U}(\eta,z),\ \bar{V} \to \left(\bar{X}/\lambda\right)^{-1/3}\tilde{V}(\eta,z), \text{(C.12)}$$

with $\tilde{W}(\eta,z),\tilde{U}(\eta,z),\tilde{V}(\eta,z)$ determined by the similarity equations(5.26)-(5.28)and (C.5)for $\bar{Y} = O(1)$ since

$$\eta \equiv Y/\left(X/\lambda\right)^{1/3} = \bar{Y}/\left(\bar{X}/\lambda\right)^{1/3}. \qquad \text{(C.13)}$$

This is precisely the asymptotic behavior that the near field solution constructed GSDC-1and GSDC-2 would have had if the decay exponent α were taken to be 4/3 (instead of 5/3) in the main boundary layer asymptotic solution (4.1), and (4.3)-(4.5) of GSDC-2 with the explicit form of the spanwise mean terms determined by using the small k asymptotic expansion of $\pi_0(y,k)$ given by (A7) of GSDC-1. This corresponds to the fully nonlinear case, which must satisfy (C.10) and was, therefore, precluded in GSDC-1and GSDC-2 by the requirement that the near field pressure vanish at downstream infinity. The present result shows that the required pressure decay is actually produced by the outer solution which applies on the long triple deck length scale $X = O(1)$ and eventually exhibits the asymptotic behavior (5.14)-(5.21)and (5.25) as $X \to \infty$.

An alternative approach was used by Smith (1973) and Smith, Brighton, Jackson, and Hunt (1981) to embed a short (boundary layer length scale) two-dimensional hump in an outer triple-deck solution. Their analysis, which is based on shrinking a triple deck scale roughness element down to a short boundary layer length scale element, indicates that the roughness (hump) behaves like a small amplitude (i.e. small h) element with delta function shape in so far as the outer scale flow is concerned and they conclude from this that the flow must be linear. The present result shows that the corresponding outer flow can, at least in principal, be nonlinear in the three dimensional case. A complete proof would require that a numerical solution to the governing equations be constructed, which is beyond the scope of the present paper where the focus is on elongated roughness elements. The present analysis does not seem to apply to the

two dimensional flow considered by Smith. In fact Ruban & Kravtsova (2013) argue that the nonlinear wake behavior is associated with the rollup of streamwise vortices.

References

Abramowitz, M. and Stegun, I. A., 1965, Handbook of Mathematical Functions, National Bureau of Standards, Washington.

Acarlar, M.S., and Smith, C.R., 1987, A Study of Hairpin Vortices in a Laminar Boundary Layer. Part 1. J. Fluid Mech., Vol. 175, pp. 1-42.

Andersson, P., Berggren, M., and Henningson, D.S., 1999, Optimal Disturbances and Bypass Transition in Boundary Layers, Phys. Fluids, Vol. 11, No. 1, pp. 134-150.

Bender, C. M. and Orszak, S. A., 1978, Advanced Mathematical Methods for Scientists and Engineers, McGraw-Hill Book Co. New York.

Bogolepov, V. V. and Lipatov, 1985, Locally three-dimensional laminar flows, J. Appl. Mech. Tech. Phys, Vol. **26,** pp. 24-31.

Bogolepov, V. V., 1985, General arrangement of flow regimes for spatially local flows, J. Appl. Mech. Tech. Phys, Vol. **28,** pp. 860-869.

Bogolepov, V. V., 1988, Small perturbations of a laminar boundary layer, J. Appl. Mech. Tech. Phys, Vol. **29,** pp. 706-716.

Carrier, G. F., Krook, M. & Pearson, C. E., 1966, Functions of a Complex Variable, McGraw-Hill.

Case, K. M., 1960, Stability of Plane Couette Flow, Phys. Fluids, Vol. 3, pp. 143-148.

Choudhari, M. and Fischer, P., 2005, Roughness Induced Transient Growth, AIAA paper 2005-4765.

Choudhari, M. and Duck, P. W., 1996, Nonlinear Excitation of Inviscid Stationary Vortex Instabilities in Boundary Layer Flow in IUTAM Symposium on Nonlinear Instability and Transition in Three-dimensional Boundary Layers (Proceedings of the IUTAM Symposium held in Manchester, U.K. 17-20 July 1995) P.W. Duck and P. Hall eds. Kluwer Academic Publishers.

Downs, R. S., III and Fransson, J. H., M., 2014, Tollmien-Schlichting Wave Growth Over Spanwise-Periodic Surface Patterns, J. Fluid Mech., Vol. 754, pp. 39-74.

Duck, P. W. & Burggraf, O. R., 1986, Spectral solution for three-dimensional triple-deck flow over surface topography, J. Fluid Mech., Vol.162, pp.1-21.

Ellingson, T. and Palm, E., 1975, Stability of Linear Flow, Phys. Fluids, Vol. 18, pp. 487-488.

Ergin, F.G. and White, E.B., 2006, Unsteady Transitional Flows Behind Roughness Elements, AIAA Journal, Vol. 44, No. 11, pp. 2504-2514.

Fransson, J. H. M., Brandt, L., Talamelli, A. & Cossu, C., 2004, Experimental and theoretical investigation of the non-modal growth of steady streaks in a flat plate boundary layer. Phys. Fluids, Vol. 16, No. 10, pp. 3627–3638.

Fransson, J. H. M. and Talamelli, A., 2012, On the generation of steady streamwise streaks in flat-plate boundary layers, J. Fluid Mech., Vol. 698, pp. 211–234.

Goldstein, M. E., 2014, Effect of free stream turbulence on boundary layer transition, Phil. Trans. of the Royal Soc., Vol. 372, No. 2020, 20130354.

Goldstein, M.E. & Wundrow, D.W., 1965, Interaction of oblique instability waves with weak streamwise vortices, J. Fluid Mech., Vol. 284, pp.377-407.

Goldstein M. E., Sescu, A., Duck P. W., and Choudhari, M., 2010, The Long Range Persistence of Wakes Behind a Row of Roughness Elements, J. Fluid Mech**.** Vol. 644, pp. 123-163.

Goldstein M. E., Sescu, A., Duck P. W., and Choudhari, M., 2011, Algebraic/transcendental disturbance growth behind a Row of Roughness Elements, J. Fluid Mech**.,** Vol. 668, pp. 236-266

Harlow, F. H. & Welch, J. E., 1965, Numerical calculation of time-dependent viscous incompressible flow of fluid with free surfaces. *Phys. Fluids* **8**, 2182-2189

Jameson, A., 1991, Time dependent calculations using multigrid, with applications to unsteady flows past airfoils and wings, AIAA paper 91-1596

Kemp, N. H., 1951, The laminar Three-Dimensional Boundary Layer and the Study of the Flow Past a Side Edge, MAes Thesis, Cornell University.

Klebanoff, P., Cleveland, W.G., and Tidstrom, K.D., 1992, On the Evolution of a Turbulent Boundary Layer Induced by a Three-Dimensional Roughness Element, J. Fluid Mech., Vol. 237, pp. 101-187.

Landahl, M.T., 1980, A Note on an Algebraic Instability of Inviscid Parallel Shear Flows, J. Fluid Mech., Vol. 98, pp. 243-251.

Lighthill, M.J., 1964, Fourier Analysis and Generalized functions, Cambridge University Press.

Luchini, P., 2000, Reynolds-Number-Independent Instability of the Boundary Layer over a Flat Surface: Optimal Perturbations, J. Fluid Mech., Vol. 404, pp. 289-309.

Ruban, A. I. and Kravtsova, M. A. 2013, Generation of steady longitudinal vortices in hypersonic boundary layer, J. Fluid Mech., Vol. 729, pp. 702-730.

Siconolfi, L. Camarri, S. & Franson, J.M. H., 2015 Stability analysis of boundary layers controlled by miniature vortex generators, J. Fluid Mech., Vol. 784, pp. 596-618

Smith, F. T, 1973, Laminar Flow over a small hump on a flat plate, J. Fluid Mech., Vol. 57,pp. 803-824

Smith, F. T, Brighton, P. S., Jackson, P. S. and Hunt, J. C. R., 1981, On boundary layer flow over two dimensional obstacles, J. Fluid Mech., vol. 113, pp 123-152,

Stuart, J. T. 1965, The production of intense shear layers by vortex stretching and convection. NATO AGARD report 514, pp. 1-29. (Also National Phys. Lab. Aeronaut. Res. Rep. 1147).

Tumin, A. and Reshotko, E., 2001, Spatial Theory of Optimal Disturbances in Boundary Layers, Phys. Fluids, Vol. 13, No. 7, pp. 2097-2104.

Van Dyke, M., 1975, Perturbation Methods in Fluid Mechanics, The Parabolic Press, Stanford, Cal.

White, E.B. and Ergin, F.G., 2003, Receptivity and Transient Growth of Roughness-Induced Disturbances, AIAA Paper 2003-4243.

Wu, X. & Luo, J, 2003 Linear and nonlinear instabilities of a Blasius boundary layer perturbed by streamwise vortices. Part 1. Steady streaks, Journal of Fluid Mechanics, Volume 483, pp 225 – 248

YOUNG, D. M., 1954, Iterative methods for solving partial difference equations of elliptic type. *Transactions of the American Mathematical Society,* 76, 92-11.